

# Targeting TNK2/ACK1 reverses the immunosuppressive tumor microenvironment and synergizes with immunotherapy in pancreatic cancer

---

Received: 12 June 2024

---

Accepted: 24 November 2025

---

Published online: 06 December 2025

---

 Check for updates

---

Chao Wu<sup>1,2,3,4,5,13</sup>, Weishuai Liu<sup>2,3,4,5,6,13</sup>, Xiangting Hu<sup>1,2,3,4,5,13</sup>,  
Yongjie Xie<sup>1,2,3,4,5,13</sup>, Shengnan Li<sup>7,13</sup>, Xinyue Liu<sup>1,2,3,4,5</sup>, Zhaojun Sun<sup>1,2,3,4,5</sup>,  
Xiaoling Li<sup>8</sup>, Xin Yu<sup>1,2,3,4,5</sup>, Yudong Yuan<sup>1,2,3,4,5</sup>, Yiping Zou<sup>1,2,3,4,5</sup>, Ran An<sup>1,2,3,4,5</sup>,  
Yanan Chen<sup>9</sup>, Hailong Wang<sup>2,3,4,5,10</sup>, Yukuan Feng<sup>1,2,3,4,5</sup>, Song Gao<sup>1,2,3,4,5</sup>,  
Hongwei Wang<sup>1,2,3,4,5</sup>, Yifei Wang<sup>1,2,3,4,5</sup>, Nan Wang<sup>1,11,12</sup>, Chao Yang<sup>1,2,3,4,5</sup>,  
Jun Yu<sup>1,2,3,4,5</sup>, Peiqing Sun<sup>11,12</sup> ✉, Chongbiao Huang<sup>1,2,3,4,5</sup> ✉,  
Antao Chang<sup>1,2,3,4,5</sup> ✉ & Jihui Hao<sup>1,2,3,4,5</sup> ✉

---

Pancreatic ductal adenocarcinoma (PDAC) remains highly lethal due to its aggressive nature and limited treatment options, with the efficacy of immunotherapy constrained by a uniquely immunosuppressive tumor microenvironment (TME). In this study, we identify TNK2/ACK1 as a key regulator of the immunosuppressive TME in PDAC. TNK2/ACK1 is significantly upregulated in PDAC, at least in part via gene amplification and KRAS-G12 mutations. Mechanistically, TNK2/ACK1 directly phosphorylates and activates STAT5A to induce the expression of the immune checkpoint HVEM, which suppresses CD8<sup>+</sup> T-cell function via its receptor BTLA. Pharmacologic targeting of TNK2/ACK1 with AIM100 or (R)-9b enhances CD8<sup>+</sup> T-cell activation and cytotoxicity while reprogramming the TME. Furthermore, combining TNK2/ACK1 inhibitors with anti-PD-1 immunotherapy or with nab-paclitaxel plus gemcitabine demonstrates promising antitumor efficacy in both allograft and spontaneous PDAC models. Overall, our findings reveal a mechanism of immune evasion and provide a potential framework for developing tailored immunotherapeutic strategies in PDAC.

Pancreatic ductal adenocarcinoma (PDAC) is a highly lethal malignancy of the digestive system with a dismal prognosis. In addition to the rising incidence of PDAC, the 5-year overall survival rate (OS) has remained stagnant at around 11%. PDAC is thus expected to become the second most common cause of cancer-related deaths by 2030<sup>1,2</sup>. Less than 20% of PDAC patients are eligible for surgical resection at the time of diagnosis due to the lack of early symptoms and the

aggressiveness of this disease<sup>3,4</sup>. Chemotherapy based on gemcitabine (GEM) is currently the standard treatment for most patients, especially those with metastatic PDAC, but has limited survival benefit and high toxicity. In recent years, immune checkpoint blockers (ICB) targeting PD-L1/PD-1 or CTLA-4 have shown remarkable efficacy in immunogenic tumors such as melanoma, non-small cell lung cancer, and hepatocellular carcinoma, significantly prolonging patient survival<sup>5-7</sup>.

---

A full list of affiliations appears at the end of the paper. ✉ e-mail: [psun@wakehealth.edu](mailto:psun@wakehealth.edu); [chhuang@tmu.edu.cn](mailto:chhuang@tmu.edu.cn); [changantao@tjmuch.com](mailto:changantao@tjmuch.com); [haojihui@tjmuch.com](mailto:haojihui@tjmuch.com)

Unfortunately, multiple clinical trials have demonstrated that PDAC, as a typical immunologically “cold” tumor, did not respond to ICB, either as monotherapy or in combination with Gem-based chemotherapy<sup>8,9</sup>. The tumor microenvironment (TME) plays a critical role in the development, progression, and metastasis of PDAC, as well as in the responses to immunotherapy<sup>10,11</sup>. However, the molecular mechanisms driving the formation of the unique immunosuppressive TME leading to immunotherapy resistance in PDAC are poorly understood. Therefore, elucidating the complex interactions between the tumor and the tumor microenvironment, including the immune system, is crucial for identifying targets for novel therapeutic strategies that serve to improve immunotherapy efficacy and the prognosis in PDAC patients.

Tyrosine Kinase Non Receptor 2 (TNK2), also known as activated Cdc42-associated kinase 1 (ACK1), is a non-receptor tyrosine kinase of the Ack family that participates in a variety of cellular processes, including signal transduction, cytoskeletal dynamics, and endocytosis<sup>12,13</sup>. Although TNK2 is not considered as an oncogenic driver and its precise biological function in cancer is likely context-dependent, aberrant activation or overexpression of TNK2 has been observed in a range of malignancies, including breast, prostate, and pancreatic cancers<sup>13–15</sup>, and activated TNK2/ACK1 correlates with poor prognosis in PDAC and promotes PDAC progression by phosphorylating AKT. More recently, emerging evidence has suggested a role of TNK2/ACK1 in regulating tumor-immune cell interactions. In the lung cancer and colon cancer cohorts in TCGA, the TNK2 levels in tumor cells correlated negatively with the abundance of immune cells, including CD8<sup>+</sup> T cells<sup>16,17</sup>; however, these studies were limited to correlations defined by dataset analysis without any functional validation or mechanistic investigations. In castration-resistant prostate cancer (CRPC), deletion of TNK2/ACK1 in T cells triggers spontaneous activation of CD8<sup>+</sup> and CD4<sup>+</sup> T cells, resulting in inhibition of growth of transplanted tumors. Meanwhile, inhibition of TNK2/ACK1 in tumor cells promotes the expression of the chemokine CXCL10, which may enhance the recruitment of active T cells and boost anti-tumor immunity<sup>18</sup>. These findings suggest that, while it may not be a universal regulator of tumor immunity, TNK2 likely contributes to immune modulation in selected cancer types.

In the current study, we focused on PDAC and investigated how different expression levels of the tumor-intrinsic TNK2/ACK1 impact the immune TME and immunotherapy responses in different PDAC patients, using a combination of bioinformatics analysis and *in vitro* and *in vivo* functional studies. We started with an integrative analysis of various high-throughput sequencing datasets, including those from spatial transcriptome sequencing, single-cell transcriptome sequencing (scRNA-seq), and RNA-seq. This analysis revealed a potential role of TNK2/ACK1 in the formation of an immunosuppressive TME in PDAC. We further carried out extensive *in vitro* and *in vivo* functional studies to validate the immunosuppressive role of TNK2/ACK1 and to define the mechanism underlying this role using isogenic cell line and mouse models of PDAC. We demonstrate that in PDAC, TNK2/ACK1 expression is increased in some tumors as compared to the other tumors and normal tissues, at least in part via gene amplification or activation of the KRAS signaling, and that manipulations of the TNK2/ACK1 level in PDAC cells alter the abundance and activity of CD8<sup>+</sup> T cells in co-cultures *in vitro* and in the TME *in vivo*. Mechanistically, TNK2/ACK1 directly phosphorylates STAT5a, a sequence-specific transcription factor of the STAT family, which induces the transcription of the immune checkpoint protein HVEM, thereby inhibiting the function of CD8<sup>+</sup> T cells through the HVEM-BTLA axis and resulting in immune evasion in PDAC. Furthermore, we showed that targeting TNK2/ACK1 with the small molecule inhibitors AIM100 or (R)-9b effectively reverses the immunosuppressive TME and inhibits tumor growth in mouse models of PDAC, alone and in a synergistic fashion with  $\alpha$ PD-1 ICB therapy and nab-paclitaxel + gemcitabine (AG) chemotherapy. This combination therapy exhibits promising anti-tumor

activity in both allograft and spontaneous tumor PDAC models. Thus, our study demonstrates that targeting TNK2/ACK1 is an effective approach to reshape the immunosuppressive TME of PDAC and provides the basis for a novel combinatorial strategy for the treatment of PDAC.

## Results

### TNK2/ACK1 expression correlates with immunosuppression and poor prognosis in PDAC

To identify key factors that contribute to immunosuppressive microenvironment of PDAC, we developed an integrative analysis approach using multiple high-throughput sequencing datasets, including spatial transcriptome sequencing data from 10 PDAC patient tissues (GSM3036911), scRNA-seq data from 13 patients of Tianjin Medical University Cancer Institute and Hospital (TJMUCH), and RNA sequencing data from tumor and adjacent tissues of 150 patients from the TCGA and normal tissues from GTex database (Fig. 1a). Initially, in a representative spatial transcriptome sequencing sample, we delineated two distinct regions in the tumor, termed “Hot\_inflammatory” and “Cold\_desert” based on the level of intratumoral CD8<sup>+</sup> T cells. We then compared the gene expression variations within these two regions, resulting in the identification of the differentially expressed gene set 1 (DEGs1) (Fig. 1b, Supplementary Fig. 1a, Supplementary Data 1). Subsequently, by integrating results from the analyses of the spatial transcriptome sequencing data in these 10 tumor samples, we classified them into “Hot\_inflammatory” and “Cold\_desert” groups based on the proportion of intratumoral CD8<sup>+</sup> T cells and the spatial relationship between CD8<sup>+</sup> T cells and tumor cells. By assessing gene expression disparities across these two groups, we identified the differentially expressed gene set 2 (DEGs2) (Fig. 1c, Supplementary Data 2). Following analysis of the spatial transcriptome sequencing data in public datasets, we performed Multiplex Immunofluorescence (mIHC) staining for CD8 and CK19 to determine the proportion of intratumoral CD8<sup>+</sup> cells in the 13 samples that had been subjected to single-cell transcriptome sequencing at TJMUCH (HRA000433). We then categorized these samples into “Hot\_inflammatory” and “Cold\_desert” subtypes based on the proportion of intratumoral CD8<sup>+</sup> T cells determined by mIHC (Supplementary Fig. 1b, c); and by comparing the transcriptome profiles of these 2 subtypes, we identified differentially expressed gene set 3 (DEGs3) (Fig. 1d, Supplementary Data 3). Additionally, by integrating TCGA-PAAD tumors and adjacent tissues with GTex normal pancreas, we identified tumor versus normal differentially expressed genes, quantified an immunosuppressive state within TCGA tumors, and defined DEG4 as the subset of differentially expressed genes positively associated with immunosuppressive state (Fig. 1e, Supplementary Data 4). By integrating the results from these 4 analyses, we found a signature highly enriched in pancreatic cancer tissues and positively associated with an immune-suppressive microenvironment (Fig. 1f). Notably, TNK2/ACK1 emerged as a top component of this signature. Given its pivotal role in tumorigenesis as a kinase, we focused our further studies on TNK2/ACK1.

Integrated analysis of TNK2/ACK1 expression in three public scRNA-seq datasets (CRA001160, GSE217845, GSE155698) revealed that TNK2/ACK1 is primarily enriched in malignant ductal epithelial cells (Supplementary Fig. 1d, e). Comparative analysis of TNK2/ACK1 expression between PDAC tissues and normal adjacent tissues (NAT) (including paired samples) across multiple databases, including TCGA, CPTAC, GEO (GSE15471, GSE151580, GSE101448, GSE71989 and GSE16515), demonstrated that TNK2/ACK1 expressed was significantly increased in PDAC tissues as compared to the normal tissues or normal adjacent tissues (Supplementary Fig. 1f–l). These findings were further supported by immunohistochemistry (IHC) staining of TNK2/ACK1 in a cohort of 70 PDAC surgical samples and their paired adjacent non-tumor tissues collected at TJMUCH, in that high expression of TNK2/ACK1 was observed in cancer as compared to normal tissues,

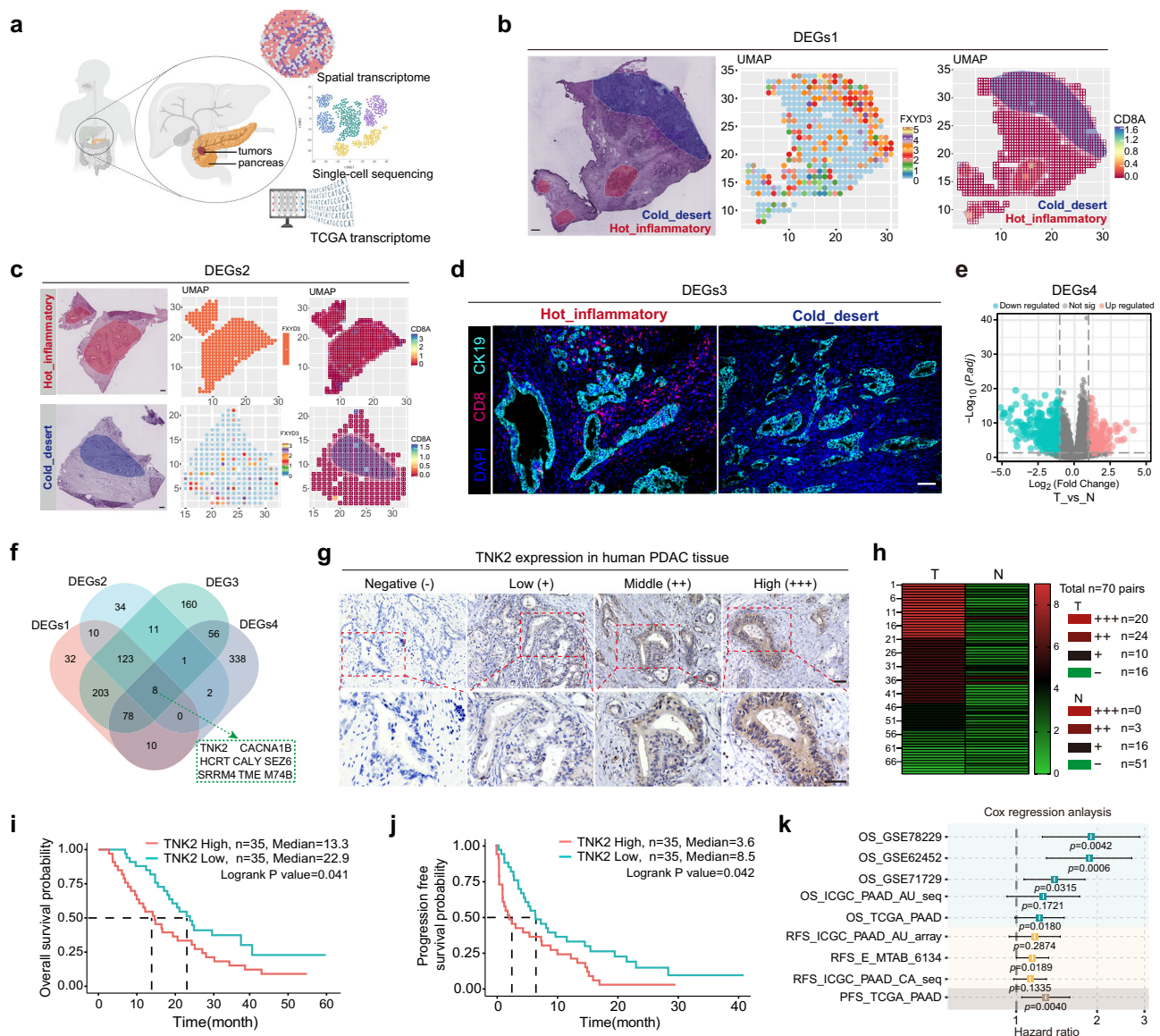


**Fig. 1 | TNK2 expression negatively correlates with immune infiltration and prognosis in PDAC.** **a** Schematic illustration of the screening strategy created in BioRender. wu, c. (2025) <https://BioRender.com/9r8yh15>.

**b** Representative spatial partition showing “Cold\_desert” zones and “Hot\_inflammatory” zones defined by CD8<sup>+</sup> T cell distribution; 120 spots were randomly sampled from “Cold\_desert” and 160 from “Hot\_inflammatory” across 10 cases (GSM3036911). Each spot diameter 50  $\mu$ m. Differential expression genes between the two spot groups are provided as DEGs1 in Supplementary Data 1.

**c** Representative images grouping into “Cold\_desert” samples and “Hot\_inflammatory” samples based on CD8<sup>+</sup> T cell infiltration across the same 10 cases (GSM3036911); differential expression genes between two groups are provided as DEGs2 in Supplementary Data 2.

**d** Representative mIHC images from 13 cases (HRA000433) illustrating “Cold\_desert” tumors and “Hot\_inflammatory” tumors. And 100 areas were randomly sampled from “Cold\_desert” tumors and 80 from “Hot\_inflammatory” tumors for CD8<sup>+</sup> T cell fraction quantification; each area diameter 100  $\mu$ m. Differential expression genes between two groups are provided as DEGs3 in Supplementary Data 3. CD8<sup>+</sup> T cells: red, CK19: cyan, nucleus: blue.

**e** DEGs4 denotes tumor versus normal differential expression genes from TCGA-PAAD and GTEx that are positively associated with the immunosuppressive state within TCGA

tumors (provided in Supplementary Data 4). **f** Venn diagram showing the intersection of tumor microenvironment with the immunosuppressive tumor microenvironment in PDAC. Four differential gene sets were intersected. Selection thresholds were: DEGs1  $\log_2FC \geq 1.5$ ,  $p < 0.05$ ; DEGs2  $\log_2FC \geq 1.3$ ,  $p < 0.05$ ; DEGs3  $\log_2FC \geq 1.5$ ,  $p < 0.05$ ; DEGs4  $\log_2FC \geq 1.0$ ,  $p < 0.05$ .

**g** The representative images of TNK2 IHC staining at different expression levels ( $n = 70$  independent samples).

**h** The heatmap of the differential expression of TNK2 in 70 pairs of tumor tissues (T) and corresponding adjacent non-tumor tissues (N).

**i, j** Survival analysis of PDAC patients with low and high TNK2 expression based on the dataset of TJMUCH, and  $p$  value from log-rank test are shown.

**k** Statistical analysis of OS, RFS and PFS based on a multi-center retrospective cohort for TNK2 Hazard ratio (GSE78229:  $n = 49$ ; GSE62452:  $n = 65$ ; GSE71729:  $n = 125$ ; ICGC-PAAD-AU seq:  $n = 81$ ; TCGA-PAAD:  $n = 150$ ; ICGC-PAAD-AU-array:  $n = 103$ ; E-MTAB-6134:  $n = 288$ ; ICGC-PAAD-CA-seq:  $n = 113$ . All  $n$  represents independent samples). Hazard ratio with 95% confidence intervals, box shows the interquartile range (IQR), line indicates the median, and whiskers the min/max values; tests two sided; exact  $p$  values are reported in the legends. Scale bars: 100  $\mu$ m. Source data are provided as a Source Data file.

predominantly in malignant ductal epithelial cells (Fig. 1g, h). Furthermore, the expression level of TNK2/ACK1 inversely correlated with both overall survival (OS) and progression-free survival (PFS) of PDAC patients, as demonstrated in our own cohort and in several

independent public datasets (Fig. 1i–k, Supplementary Fig. 1m, n). Consistently, analysis of clinical pathological data indicated that high expression of TNK2/ACK1 was associated with poor prognosis in PDAC, as determined by univariate regression analysis, although not in

multivariate regression analysis (Supplementary Data 5–7). Together, these data demonstrate that TNK2/ACK1 is expressed at high levels in PDAC as compared to normal tissues and is associated with immunosuppression and poor patient prognosis.

### Increased TNK2/ACK1 expression is driven at least in part by gene amplification and KRAS-G12 mutations in PDAC

TNK2 expression is increased in tumor tissues of PDAC as compared to normal tissues and varies considerably among different tumors (Supplementary Fig. 1c–i). For example, the TNK2 expression levels [ $\log_2$  (TPM + 1)] varied in a range of 3.4 folds among different PDAC patients in the TCGA cohort (Supplementary Fig. 1f). We thus studied the potential molecular mechanisms driving the upregulation of TNK2/ACK1 in PDAC. Analysis of copy number variation (CNV) data from three independent datasets revealed that a subset of tumors harbored different levels of copy number gains of the TNK2 locus. Specifically, high-level amplification of TNK2 (defined as gain of  $\geq 2$  additional copies) was detected in 3.6%, 2.7%, and 9.2% of the PDAC samples, and low-level amplification (gain of 1 additional copy) was observed in 17.9%, 13.5%, and 38.9% of the samples, from the CPTAC, TCGA, and UTSW (PRJNA278883) datasets, respectively (Supplementary Fig. 2a).

Furthermore, a positive correlation was observed between TNK2/ACK1 expression and the copy number of the TNK2 gene, and tumors with either high-level or low-level amplifications showed significant increases in TNK2 expression as compared to those without, in both TCGA and CPTAC datasets (Supplementary Fig. 2b, c). Notably, patients with TNK2 gene amplification (more than 1 additional copies) exhibited significantly poorer prognosis compared to those without such alterations (Supplementary Fig. 2d). To conform these findings, we conducted fluorescence in situ hybridization (FISH) analysis of TNK2 using specific probes in a cohort of 98 PDAC surgical specimens collected at our center. We observed TNK2 gene amplification (copy number  $\geq 2$ ) in 9.18% (9 out of 98) of the samples, which was associated with aberrantly high expression of TNK2/ACK1 and significantly worse survival outcomes in these patients (Supplementary Fig. 2e–g).

Immunohistochemical staining for TNK2/ACK1 in our cohort of 70 PDAC patients revealed that TNK2/ACK1 was expressed at moderate to high levels in 62.9% (44/70) of cases, a rate that far exceeds the observed frequency of gene amplification (Fig. 1j, k). This suggests that mechanisms beyond gene amplification may contribute to the upregulation of TNK2/ACK1 in PDAC. Notably, we observed a significant association between elevated TNK2/ACK1 expression and the presence of KRAS mutations, one of the most common genetic alterations in PDAC, in the TCGA dataset (Supplementary Fig. 3a). And the analysis of the TCGA-PAAD dataset and a single cell RNA-seq dataset for PDAC (GSE155698) revealed significant positive correlations ( $R = 0.40$  and  $R = 0.38$ , respectively) between TNK2 expression and the KRAS dependency signature<sup>19</sup> in PDAC tumor cells (Supplementary Fig. 3b, c). We further examined the correlation between TNK2/ACK1 expression and specific subtypes of KRAS mutations across three independent datasets (TCGA, CPTAC, and UTSW). These analyses revealed a significant positive correlation of TNK2/ACK1 expression with overall KRAS-G12 mutations (Supplementary Fig. 3d, f, h, j) and with KRAS-G12D, G12R and G12V mutations (Supplementary Fig. 3e, g, i) in all 3 datasets. However, the correlation between TNK2 and some of the other KRAS mutations, such as G12S and mutations at positions 13, 23, 60 and 62, cannot be determined due to the limited number of cases with these mutations. Additionally, stratification of patients by TNK2/ACK1 expression levels within the TCGA dataset revealed that the KRAS mutation rate was 86.7% in the TNK2/ACK1-high expression group, as compared to 45.3% in the TNK2/ACK1-low expression group (Supplementary Fig. 3k). Consistently, Western blotting analysis indicated that TNK2/ACK1 expression was significantly higher in most KRAS-G12 mutant cell lines compared to KRAS wild-type (WT) cell lines

(Supplementary Fig. 3l). In an effort to establish the causative link of the KRAS-G12 mutations to TNK2 upregulation, we tested the effects of a KRAS-G12D specific inhibitor MRTX1133<sup>20</sup> and the non-covalent pan-KRAS inhibitor BI-2865<sup>21</sup> on TNK2 expression in PDAC cell lines with difference KRAS mutational status, BxPC-3 (KRAS wild-type), SW1990 (KRAS-G12D mutant), Capan-2 (KRAS-G12V mutant), and MIA PaCa-2 (KRAS-G12C mutant) (Supplementary Fig. 3m). Consistent with its ability to inhibit all KRAS forms, BI-2865 reduced ERK phosphorylation, and simultaneously decreased TNK2 expression, in all KRAS-G12 mutant cell lines, and had a similar although less prominent effect on ERK and TNK2 in the KRAS wild-type cell line BxPC-3. In contrast, the KRAS-G12D-specific MRTX1133 inhibited ERK phosphorylation and TNK2 expression only in the KRAS-G12D mutant cell line SW1990, but not in the other KRAS-G12 mutant cell lines or the KRAS wild-type cell line. These results indicate that upregulation of TNK2/ACK1 in PDAC is mediated at least in part by KRAS-G12 mutations, including G12D, G12V and G12C.

KRAS mutations are known to regulate gene transcription through activation of the ERK mitogen-activated protein kinase (MAPK) cascade, which governs a pro-tumorigenic network in PDAC<sup>22,23</sup>. Supporting a role of ERK in oncogenic KRAS-G12 mutant mediated TNK2/ACK1 expression, an ERK inhibitor SCH772984 significantly decreased TNK2/ACK1 expression in both Panc10.05 and SW1990 cells containing KRAS-G12D mutation (Supplementary Fig. 3n), suggesting that ERK may play a crucial role in mediating TNK2/ACK1 upregulation in response to activated KRAS signaling. Of note, since ERK inhibition suppresses cell growth in Panc10.05 cells, but not SW1990 cells, the similar effect of the ERK inhibitor on TNK2/ACK1 expression in both cell lines suggests that the ERK downstream pathway regulating TNK2/ACK1 upregulation diverges from that regulating cell growth and proliferation.

Collectively, our findings demonstrate that the upregulation of TNK2/ACK1 in some tumors of PDAC as compared to the other tumors and to the normal tissues is at least partly driven by gene amplification and oncogenic KRAS signaling mediated by the G12 mutations. It is highly likely other mechanisms, besides gene amplification and oncogenic KRAS signaling, also contribute to TNK2/ACK1 upregulation in PDAC. In addition, while we demonstrated the contribution of specific KRAS mutations, including G12D, G12V, G12R and G12C, to TNK2 upregulation based their correlation with high TNK2 levels in patient datasets and/or their requirement for TNK2 expression in wild-type and KRAS-mutant PDAC cell lines treated with KRAS inhibitors, our results do not rule out the possible involvement of other subtypes of KRAS mutations in TNK2 regulation.

### TNK2/ACK1 expression negatively correlates with intratumoral CD8<sup>+</sup> T cell infiltration

To investigate the roles of TNK2/ACK1 in the establishment of an immunosuppressive microenvironment in PDAC, we analyzed scRNA-seq data from 24 PDAC tumors (GSA: CRA001160) for cell-cell communications among ten distinct cell clusters using Cell-Chat analysis. Notably, malignant ductal epithelial cells with high TNK2 expression displayed robust communication with CD8<sup>+</sup> T cells and moderate interactions with pancreatic stellate cells (PSCs), while those with low TNK2 expression appeared to primarily interact with macrophages within the tumor microenvironment (TME) of PDAC (Fig. 2a–c, Supplementary Fig. 4a–g). miHC staining of our cohort of 98 PDAC surgical specimens revealed a significant negative correlation between TNK2/ACK1 expression and the abundance of CD8<sup>+</sup> T cells, with a correlation coefficient of  $-0.6085$  (Fig. 2d, e). Meanwhile, TNK2/ACK1 expression exhibited a low negative correlation with NK cells (NKp60<sup>+</sup> cells), a weak positive correlation with the abundance of myeloid-derived suppressor cells (MDSCs, CD33<sup>+</sup> cells), but did not influence the abundance of FOXP3<sup>+</sup> regulatory T (Treg) cells (Supplementary Fig. 4h–j). Additionally, correlation analysis of single-cell RNA

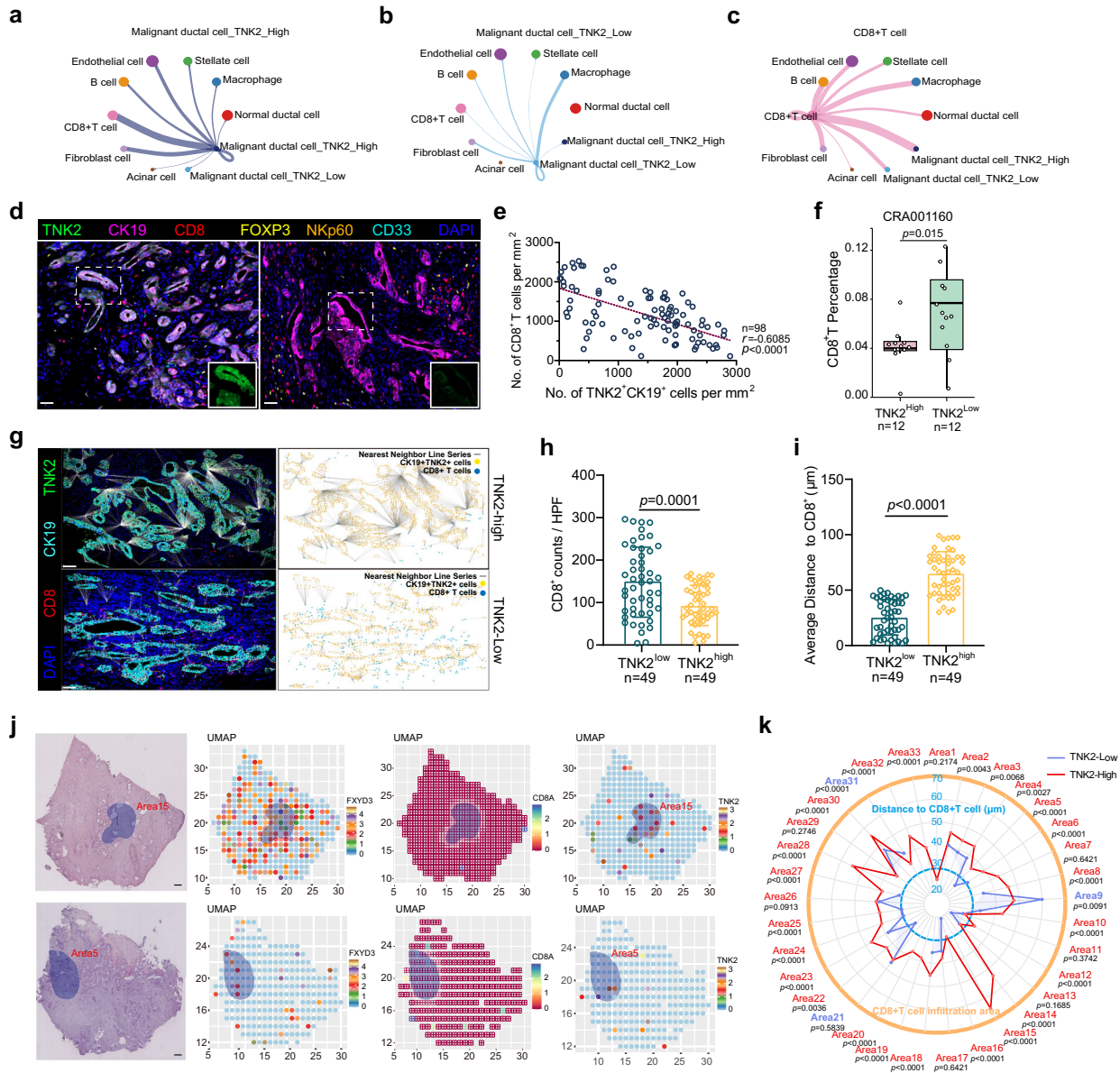


**Fig. 2 | TNK2 crosslinks with CD8<sup>+</sup> T cells in the TME of PDAC TME.**

**a–c** Interactions of the TNK2<sup>high</sup> Malignant ductal cells. **a** TNK2<sup>low</sup> Malignant ductal cells (**b**) and CD8<sup>+</sup> T cells (**c**) with other cell types indicated in the figure, as determined by cell-cell contact analysis. **d** Representative images of the mIHC staining of PDAC tissue microarray ( $n = 98$  independent samples) with high (left) or low (right) TNK2 expression. Images are representative of results observed across the cohort. CD8<sup>+</sup> T cells: red, NK cells (NKp60<sup>+</sup> cells): orange, MDSC cells (CD33<sup>+</sup> cells): cyan, Tregs (Foxp3<sup>+</sup> cells): yellow, CK19<sup>+</sup> cells: pink, and nuclei: blue. Scale bars: 50  $\mu\text{m}$ . **e** Correlation between counts of TNK2<sup>+</sup>CK19<sup>+</sup> cells and counts of CD8<sup>+</sup> T cells in PDAC samples ( $n = 98$  independent samples). The  $r$  value was determined based on the spearman correlation coefficient, two-sided  $p$  value is reported. **f** Correlation between tumor-cell TNK2 expression and the percentage of CD8<sup>+</sup> T cells was assessed using the single-cell RNA-seq dataset CRA001160 ( $n = 24$  independent primary PDAC tumors). Tumors were stratified by the median tumor-

cell TNK2 expression into TNK2-High and TNK2-Low groups (12 cases each). **g** The representative mIHC staining images of PDAC tissue microarray (left) ( $n = 98$  independent samples) with TNK2 in green, CK19 in cyan, CD8<sup>+</sup> T cell in red and nuclei in blue, the closest spatial distance analysis (right) with TNK2<sup>+</sup>CK19<sup>+</sup> cells in yellow dots and CD8<sup>+</sup> T cells in blue dots, the lines were the connections between them. Scale bars: 50  $\mu\text{m}$ . The statistical analysis of the number of CD8<sup>+</sup> T cells (**h**) and the nearest distance between TNK2<sup>+</sup>CK19<sup>+</sup> cells and CD8<sup>+</sup> T cells (**i**) in PDAC samples with different TNK2 expression. Analysis of the TNK2 expression from 33 randomly selected regions on 10 spatial transcriptome sequencing samples (**j**) and the average distance of the nearest CD8<sup>+</sup> T cells in these selected regions (**k**). Two-sided Welch  $t$  test with Benjamini–Hochberg correction; adjusted  $p$  values are indicated (**k**). Scale bars: 50  $\mu\text{m}$ . Statistical significance was determined by two-sided Wilcoxon rank-sum tests (**f**, **h**, **i**), box shows the interquartile range (IQR), line indicates the median, and whiskers the min/max values. Source data are provided as a Source Data file.

sequencing datasets CRA001160 ( $n = 24$ ) and GSE202051 ( $n = 43$ ) revealed a significant negative correlation between TNK2 expression in pancreatic cancer cells and CD8<sup>+</sup> T cells (Fig. 2f, Supplementary Fig. 4k). Also, the deconvolution analysis of the TCGA database revealed a significant negative correlation between TNK2 expression in pancreatic cancer cells and CD8<sup>+</sup> T cells, with a correlation coefficient of  $-0.75$  (Supplementary Fig. 4l). Further, to gain a more

comprehensive understanding of the relationship between TNK2 expression and CD8<sup>+</sup> T cell infiltration, we employed several widely used immune infiltration analysis methods<sup>24</sup>, including TIMER, MCPcounter, xCell, CIBERSORT-ABS, and Quantiseq, across multiple datasets. Consistently, these analyses demonstrated a robust negative correlation between TNK2 expression and CD8<sup>+</sup> T cell infiltration across the different datasets (Supplementary Fig. 4m).

To evaluate the impact of TNK2/ACK1 on the spatial distribution of CD8<sup>+</sup> T cells, we analyzed the average distance between TNK2/ACK1<sup>+</sup> CK19<sup>+</sup> tumor cells and CD8<sup>+</sup> T cells. While samples with high TNK2/ACK1 expression displayed significantly lower abundance of CD8<sup>+</sup> T cells as compared to those with low TNK2/ACK1, as expected, the average distance between tumor cells and CD8<sup>+</sup> T cells was notably greater in the high-expression group than in the low-expression group (Fig. 2g–i, Supplementary Fig. 4n). Interestingly, the proportion of intratumoral CD8<sup>+</sup> T cells in samples with TNK2 amplification was much lower than in those without, and the average distance between tumor cells and CD8<sup>+</sup> T cells was substantially larger in samples with TNK2 amplification (Supplementary Fig. 4o, p). Moreover, we randomly selected 33 regions of 10 PDAC patients from spatial transcriptome sequencing datasets and analyzed the correlation between TNK2 expression levels in PDAC cells and the distance from and the quantity of surrounding CD8<sup>+</sup> T cells. Remarkably, in most regions (24 out of 33), tumor cells with high TNK2 expression had a lower density of surrounding CD8<sup>+</sup> T cells and were situated farther away from them as compared to those with low TNK2 expression (Fig. 2j, k). In summary, our findings suggest that tumor cells expressing high levels of TNK2/ACK1 may suppress CD8<sup>+</sup> T cells infiltration and antitumor function, thereby promoting the establishment of an immunosuppressive microenvironment in PDAC.

### TNK2/ACK1 impairs CD8<sup>+</sup> T cell function to promote PDAC progression

As TNK2/ACK1 has been reported to promote tumor cell proliferation in various types of cancer by regulating multiple signaling pathways through its kinase activity<sup>13,15,25–28</sup>, we investigated whether TNK2/ACK1 influenced the proliferation of PDAC cells. Interestingly, during the culture of PDAC organoids, we observed no significant difference in growth rate between organoids with high TNK2/ACK1 expression and those with low TNK2/ACK1 (Supplementary Fig. 5a–c). Furthermore, neither ectopic expression of TNK2 in TNK2/ACK1-low organoids (PDAC#5) nor shRNA-mediated knockdown of TNK2 in TNK2/ACK1-high organoids (PDAC#4) affected the size of the organoids and the proportion of Ki67<sup>+</sup> proliferating cells (Supplementary Fig. 5d–g), suggesting that TNK2/ACK1 has no effect on the growth of PDAC organoids. In three murine PDAC cell lines (KPC#1, KPC#2 and KPC#3) with different TNK2/ACK1 expression levels, generated from spontaneous tumors from the KPC (LSL-KrasG12D/+Trp53R172H/+Pdx1-Cre+/-) mice in our lab, we exogenously overexpressed TNK2 in the KPC#3 cell line with low TNK2/ACK1 expression, and knocked down TNK2 in KPC#1 cell line with high TNK2/ACK1 expression (Supplementary Fig. 5h–k). Consistently, neither overexpression nor knockdown of TNK2 influenced the growth of KPC cells (Supplementary Fig. 5l, m). Together with our previous data showing that TNK2/ACK1-high PDAC cells communicate with CD8<sup>+</sup> T cells and impair their abundance in the TME, we hypothesize that TNK2/ACK1 inhibits the activity of CD8<sup>+</sup> T cells, facilitating the formation of an immunosuppressive microenvironment, and thereby promoting PDAC progression.

To test this hypothesis, we constructed pancreatic orthotopic xenograft tumor models using KPC#1 cell lines with TNK2 knockdown or scramble control in wild type C57BL/6 mice or C57BL/6 mice with CD8<sup>+</sup> T cells depletion (Supplementary Fig. 6a, b), or Balb/c nude mice. As expected, in immunocompetent C57BL/6 mice, knockdown of TNK2 significantly impeded the growth of orthotopic allograft tumors, while depletion of CD8<sup>+</sup> T cells entirely nullified the tumor growth suppression induced by TNK2 knockdown; consistently, in T cell-deficient Balb/c nude mice, TNK2 knockdown had no impact on tumor growth in orthotopic xenograft tumor models (Fig. 3a–c, Supplementary Fig. 6c). These findings indicate that CD8<sup>+</sup> T cells are necessary for the suppression of tumor growth by loss of TNK2/ACK1.

Next, we explored the effect of the TNK2/ACK1 levels in tumor tissues on immune cell abundance and function, using the orthotopic

allograft tumor models formed by KPC#3 cell lines with TNK2 overexpression or KPC#1 cell lines with TNK2 knockdown. TNK2 knockdown in KPC#1 cells hindered the growth of allograft tumors, consistent with the results in Fig. 3a–c, while TNK2 overexpression in KPC#3 facilitated the tumor growth (Fig. 3d–f, Supplementary Fig. 6d). Subsequently, we employed a 21-color flow cytometer to analyze the proportions of various major immune cells, such as CD8<sup>+</sup> T cells, NK cells, and others within the tumor tissues (Supplementary Fig. 7a). We found that TNK2 overexpression significantly reduced the abundance of CD8<sup>+</sup> T cells in the tumor tissue, mildly reduced NK cell abundance, and slightly increase the abundance of MDSCs and Treg cells (Fig. 3g, Supplementary Fig. 7b–h). Moreover, TNK2 overexpression markedly suppressed the cytotoxic activity of CD8<sup>+</sup> T cells, and promoted their exhaustion, as evidenced by reduced expression of the cytotoxic effector Granzyme B and cytokine TNF- $\alpha$ , and increased expression of exhaustion markers PD-1 and TIM3, respectively (Fig. 3h–k). Conversely, TNK2 knockdown increased the abundance of CD8<sup>+</sup> T cells, bolstered their cytotoxic activity, alleviated their exhaustion, mildly increased NK cells, and slightly reduced MDSC and Treg cell infiltration (Fig. 3g–k, Supplementary Fig. 7b–h). Overall, the results from these *in vivo* functional studies indicate that TNK2/ACK1 promotes immune evasion and progression of PDAC at least partly through inhibiting the abundance and function of CD8<sup>+</sup> T cells.

### TNK2/ACK1 inhibits CD8<sup>+</sup> T cell activity through direct cell-to-cell contact

To further investigate the influence of TNK2/ACK1 on CD8<sup>+</sup> T cell activity, naïve CD8<sup>+</sup> T cells were isolated from the spleens of immunocompetent C57BL/6 mice, activated using  $\alpha$ CD3/ $\alpha$ CD28 Dynabeads along with IL-2, and then directly co-cultured with KPC cells with overexpression or knockdown of TNK2 at a ratio of 10:1 (Fig. 4a). Flow cytometric analysis revealed that co-culture with TNK2-overexpressing KPC#3 cells significantly suppressed the secretion of cytokines TNF $\alpha$ /IFN- $\gamma$  and cytotoxic effector Granzyme B, induced exhaustion, and consequently inhibited the proliferation of CD8<sup>+</sup> T cells; in contrast, after direct co-culture with KPC#1 cells with TNK2 knockdown, CD8<sup>+</sup> T cells displayed a significant increase in the secretion of effector cytokines, a decrease in exhaustion, and enhancement in proliferation (Fig. 4b–d, Supplementary Fig. 8a–e). However, in an indirect co-culture system, neither overexpression nor knockdown of TNK2 had an impact on the proliferation and function of CD8<sup>+</sup> T cells (Supplementary Fig. 8f–n), suggesting that the inhibition of CD8<sup>+</sup> T cell function by TNK2/ACK1 in tumor cells requires direct contact between tumor cells and CD8<sup>+</sup> T cells.

Furthermore, we directly co-cultured CD8<sup>+</sup> T cells isolated from the spleens of OT-1-td-Tomato mice with KPC cells overexpressing ovalbumin (OVA), followed by TNK2 overexpression (KPC#3) or knockdown (KPC#1), to assess the impact of TNK2/ACK1 on the cytotoxicity of CD8<sup>+</sup> T cells (Fig. 4e). Remarkably, overexpression of TNK2 in KPC#3 cells suppressed the cytotoxic activity of CD8<sup>+</sup> T cells derived from OT-1 mice, evidenced by a decrease in the proportion of apoptotic tumor cells measured via flow cytometry analysis of annexin-V and PI and immunofluorescent staining of Caspase3/7 (Fig. 4f–i), as well as a reduction in tumor cells lysed by CD8<sup>+</sup> T cells detected through LDH release analysis (Fig. 4j). Conversely, knockdown of TNK2 in KPC#1 cells significantly enhanced the cytotoxic activity of OT-1-derived CD8<sup>+</sup> T cells (Fig. 4f–j). To further investigate the inhibitory effect of TNK2/ACK1 on the tumor-specific cytotoxicity of CD8<sup>+</sup> T cells, we constructed PDAC organoids with either TNK2 overexpression or knockdown and directly co-cultured them with pre-activated PBMCs from the same patient (Fig. 4k). Consistently, TNK2 overexpression inhibited the cytotoxic effect of autologous PBMCs against PDAC cells, while TNK2 knockdown had the opposite effect (Fig. 4l, m). Taken together, the results from these *in vitro* functional studies demonstrate that TNK2/ACK1 in tumor cells impairs CD8<sup>+</sup> T cell mediated antitumor immunity through direct cell-to-cell contact.

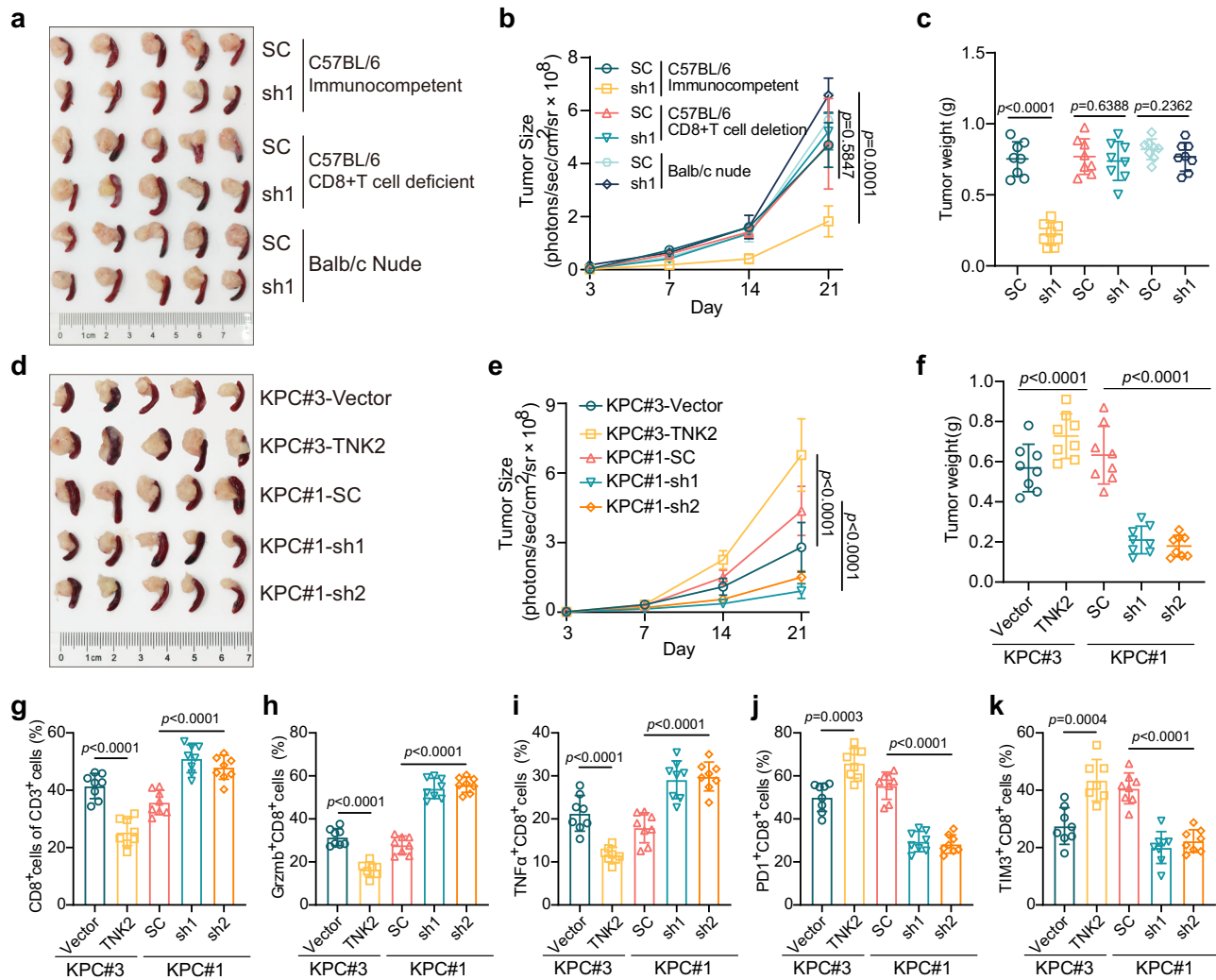


**Fig. 3 | Targeting TNK2 suppresses tumor growth in a CD8<sup>+</sup> T cell-dependent fashion.** **a–c** Representative pancreatic tumor images at the endpoint of indicated KPC cells orthotopic grafted into immunocompetent or CD8<sup>+</sup>T cell deficient C57BL/6 mice or BALB/c nude mice ( $n = 8$  independent experiments) (a). Tumor growth curves (b) and tumor weights (c) measured at the endpoint. **d** Representative pancreatic tumor images at the endpoint of indicated KPC cells orthotopic transplanted into C57BL/6 mice ( $n = 8$  independent experiments) (d). Tumor growth

curves (e) and tumor weights (f) measured at the endpoint. Flow cytometry analysis showing the changes of CD8<sup>+</sup> T cells (g), GzmB<sup>+</sup>CD8<sup>+</sup> T cells (h), TNF<sup>+</sup>CD8<sup>+</sup> T cells (i), PD-1<sup>+</sup>CD8<sup>+</sup> T cells (j) and TIM3<sup>+</sup>CD8<sup>+</sup> T cells (k) in each group ( $n = 8$  independent experiments). Statistical significance was determined by two-way ANOVA followed by Tukey's multiple comparisons test (b, e) and one-way ANOVA followed by Tukey's multiple comparisons test (c, f–k). All tests were two sided. Data represents mean  $\pm$  s.d. Source data are provided as a Source Data file.

### HVEM is required for TNK2/ACK1-mediated inhibition of CD8<sup>+</sup> T cells

Since TNK2/ACK1 is an intracellular non-receptor tyrosine kinase, and its expression in tumor cells inhibits CD8<sup>+</sup> T cell activity through direct cell-to-cell contact, we reasoned that TNK2/ACK1 might regulate specific immune regulatory factors on the cell surface of the tumor cells to suppress the activity of CD8<sup>+</sup> T cells. To identify such effectors, we performed quantitative mass spectrometry analysis of the membrane proteins from TNK2-overexpressing and control KPC#3 cells, which identified a set of proteins regulated by TNK2/ACK1 (Supplementary Data 8). We performed intersection analysis of these proteins with immune regulatory factors, cell membrane proteins, and genes upregulated in PDAC (fold change  $\geq 2$ ), and identified 6 potential candidates, including HVEM, PPIA, GPI, PSMC2, CALR and RAC1 (Fig. 5a). Among them, HVEM showed the highest enrichment in quantitative mass spectrometry analysis, and the strongest correlation in expression with TNK2/ACK1 (coefficient = 0.53) in the TCGA database (Supplementary Fig. 9a, b). HVEM, also known as TNFRSF14 or CD270, is

a member of the tumor necrosis factor receptor superfamily and acts as a critical regulator of both innate and adaptive immune responses<sup>29,30</sup>. Therefore, we focused on HVEM, an immune checkpoint protein with increased expression in PDAC as compared to normal tissues (Supplementary Fig. 9c).

Cell Merge Density-based co-expression analysis of PDAC single-cell sequencing data (GSA: CRA001160) revealed a significant co-expression of TNK2 and HVEM in malignant ductal epithelial cells (Fig. 5b). IHC analysis in our cohort of 98 PDAC patients demonstrated a significant positive correlation between HVEM and TNK2/ACK1 expression, with coefficient of 0.5497 (Supplementary Fig. 9d, e). Furthermore, overexpression of TNK2 in both murine and human PDAC cell lines dramatically increased the protein and mRNA levels of HVEM and promoted its membrane localization, while knockdown of TNK2 markedly decreased HVEM expression and membrane localization (Supplementary Fig. 9f–i). Additionally, network centrality analysis<sup>31</sup> of the HVEM signaling pathway from PDAC single-cell sequencing data indicated that TNK2-overexpressing malignant ductal epithelial cells were the primary source/sender of the HVEM signal,

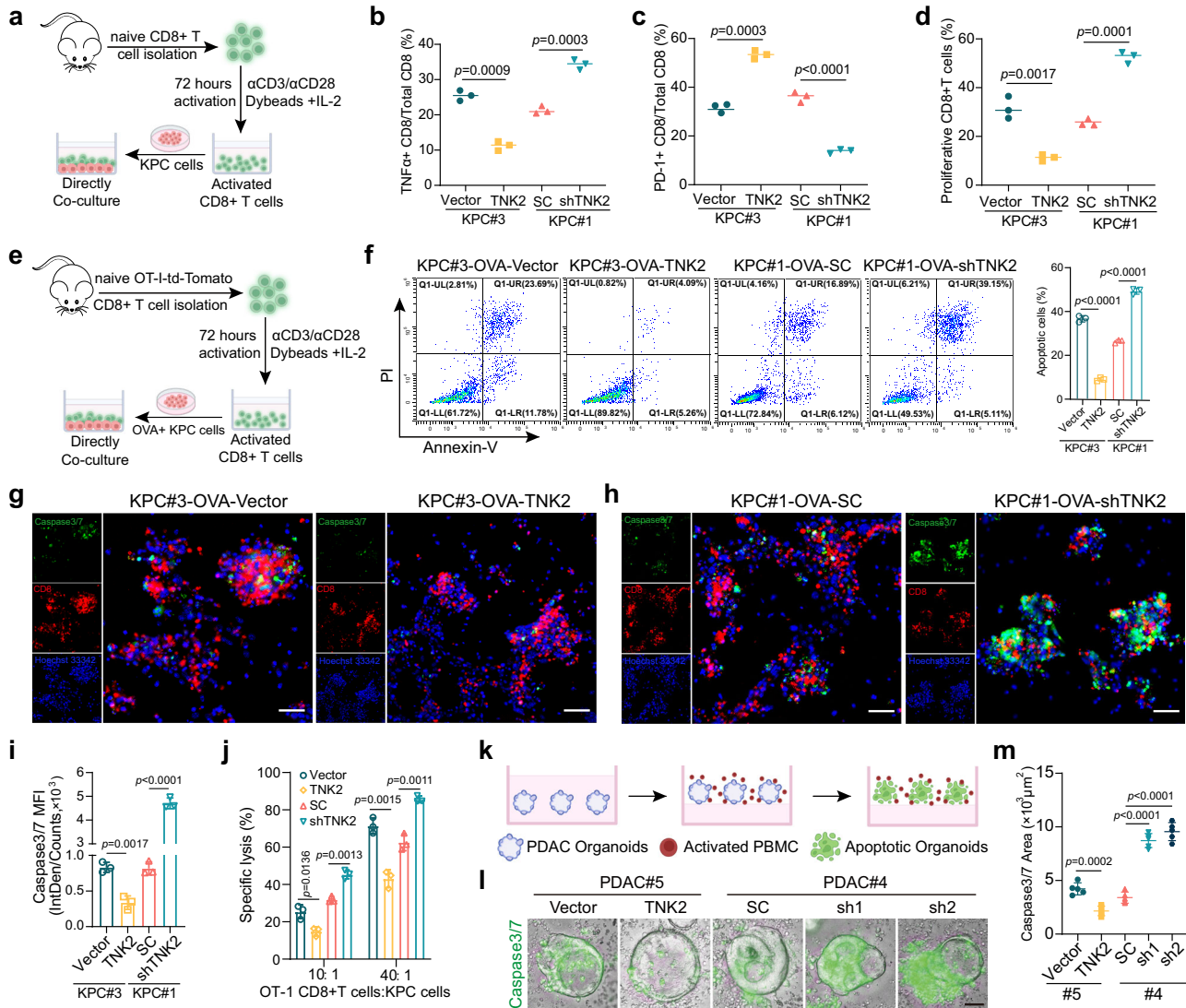


**Fig. 4 | TNK2 impaired the CD8<sup>+</sup> T cell function through cell-to-cell contact.**  
**a** Schematic illustration of the co-culture experiment for activated CD8<sup>+</sup> T cells and KPC cells created in BioRender. [wu, c. \(2025\) https://BioRender.com/9r8yhl5](https://BioRender.com/9r8yhl5). The flow cytometry analysis showing the changes of TNFα<sup>+</sup> CD8<sup>+</sup> T cells (**b**), PD-1<sup>+</sup> CD8<sup>+</sup> T cells (**c**) and proliferative CD8<sup>+</sup> T cells (**d**) in the co-culture system (*n* = 3 independent experiments). **e** Schematic illustration of the co-culture experiment for activated OT-I-td-Tomato CD8<sup>+</sup> T cell and KPC cells created in BioRender. [wu, c. \(2025\) https://BioRender.com/9r8yhl5](https://BioRender.com/9r8yhl5). **f** Percentage of apoptotic KPC#3-OVA or KPC#1-OVA cell lines after co-cultured with activated OT-I-td-Tomato CD8<sup>+</sup> T cells, as measured by flow cytometry after staining with PI and annexin-V (*n* = 3 independent experiments). The representative fluorescence images of KPC#3-OVA or

KPC#1-OVA cell lines stained with caspase-3/7 probes (green) which cocultured with OT-I-td-Tomato CD8<sup>+</sup> T cell (red) (**g**, **h**) and fluorescence intensity quantified with ImageJ (**i**) (*n* = 3 independent experiments). **j** The LDH release assay to determine the cytotoxicity of OT-I-td-Tomato CD8<sup>+</sup> T cells. **k** Schematic illustration of the apoptosis assay in PDAC organoid created in BioRender. [wu, c. \(2025\) https://BioRender.com/9r8yhl5](https://BioRender.com/9r8yhl5). The representative fluorescence images of PDAC#5 or PDAC#4 organoids stained with caspase-3/7 probes (green) which co-cultured with activated PBMC (**l**), and quantified by ImageJ (**m**) (*n* = 3 independent experiments). Scale bars, 100 μm. Statistical significance was determined by two-tailed unpaired Student's *t* test. Data represent means ± s.d. Source data are provided as a Source Data file.

while CD8<sup>+</sup> T cells were the main target/receiver (Fig. 5c, d, Supplementary Fig. 10a).

Furthermore, we knocked down HVEM in TNK2-overexpressing KPC#3 cells and then established orthotopic pancreatic tumor models in C57BL/6 mice (Supplementary Fig. 10b). HVEM knockdown significantly attenuated the enhanced tumor growth induced by TNK2 overexpression, and restored the cytotoxic activity of CD8<sup>+</sup> T cells, evidenced by increased secretion of effector cytokines, and decreased exhaustion status (Fig. 5e–i, Supplementary Fig. 10c–f). Subsequently, we established orthotopic pancreatic tumor models using KPC#1 cells with TNK2 knockdown and HVEM overexpression (Supplementary Fig. 10g). Consistently, HVEM overexpression effectively abrogated the

inhibition of tumor growth and the increase in cytotoxic activity of CD8<sup>+</sup> T cells induced by TNK2 knockdown (Fig. 5j–n, Supplementary Fig. 10h–k). Altogether, the results from these epistatic studies indicate that TNK2/ACK inhibits CD8<sup>+</sup> T cell activity by inducing HVEM in PDAC.

Interestingly, our animal experiments revealed that while HVEM was essential for TNK2/ACK1-mediated inhibition of CD8<sup>+</sup> T cell activity, it had no significant impact on TNK2/ACK1-mediated inhibition of CD8<sup>+</sup> T cell infiltration in TME (Fig. 5g, l). In vitro CD8<sup>+</sup> T cell recruitment assays indicated that TNK2 overexpression in KPC#3 cells significantly inhibited CD8<sup>+</sup> T cell recruitment, while HVEM knockdown did not reverse this effect; and consistently, HVEM

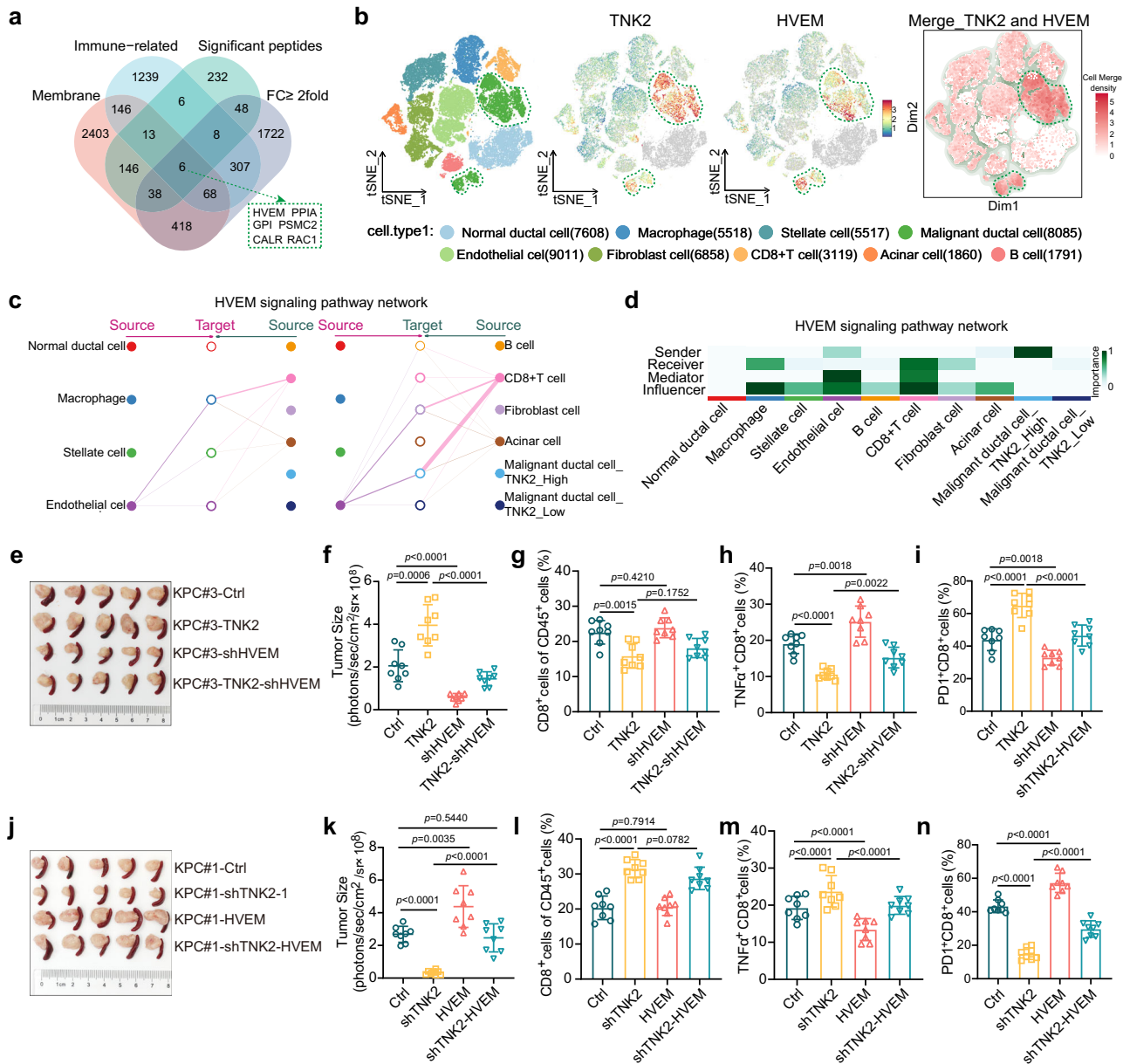


**Fig. 5 | HVEM mediates TNK2-induced CD8<sup>+</sup> T cell dysfunction.** **a** Venn diagram illustrating the screening strategy for TNK2-regulated cell surface proteins. Candidate genes were obtained from the intersection of four datasets: immune-regulatory proteins, known membrane proteins, proteins with significant membrane peptides identified by surface proteomics after TNK2 overexpression, and genes upregulated in PDAC with fold change  $\geq 2$ . Six overlapping genes (HVEM, PPIA, GPI, PSMC2, CALR, and RAC1) were identified. **b** ScRNA-seq data analysis, UMAP plot were annotated and colored for different cell types (left panel). Expression levels of TNK2 and HVEM were lighted in UMAP individually (2 middle panels) or together (right panel). **c** Hierarchical plot showing the inferred inter-cellular communication network for HVEM signaling. Solid and open circles represent source and target, respectively. Circle edge width represents the communication probability. Edge colors are consistent with the signaling source.

**d** Heatmap showing the relative importance of each cell group based on the computed four network centrality measures (Sender, Receiver, Mediator, Influencer) of HVEM signaling pathway network. Representative pancreatic tumor images (**e, j**) and tumor size measured at the experimental endpoint (**f, k**) in tumors formed by KPC#3 cells expressing TNK2 cDNA or vector (**e, f**) or KPC#1 cells expressing TNK2 shRNA or control (**j-k**). Flow cytometry analysis showing the changes of CD8<sup>+</sup> T cells (**g, l**), TNF $\alpha$ <sup>+</sup> CD8<sup>+</sup> T cells (**h, m**), and PD-1<sup>+</sup> CD8<sup>+</sup> T (**i, n**) cells in tumors formed by KPC#3 cells expressing TNK2 cDNA or vector (**g-i**) or KPC#1 cells expressing TNK2 shRNA or control (**l-n**). Statistical significance was determined by two-way ANOVA followed by Tukey's multiple comparisons test (**f, k**) and one-way ANOVA followed by Tukey's multiple comparisons test (**g-i, l-n**).  $n = 8$  independent experiments (**e-n**). All tests were two sided. Data represent as mean  $\pm$  s.d. Source data are provided as a Source Data file.

overexpression in KPC#1 cells did not prevent CD8<sup>+</sup> T cell infiltration after TNK2 knockdown (Supplementary Fig. 11a–c). These results suggest that TNK2/ACK1-induced inhibition of CD8<sup>+</sup> T cell infiltration may not be mediated by HVEM but potentially by other factors. We thus performed RNA-seq analysis in murine KPC#3 and human L3.7 PDAC cells overexpressing TNK2 or control. Gene Ontology (GO, Molecular Function) analysis of differentially expressed genes from

RNA-seq revealed that the chemokine activity (GO:0008009) and cytokine activity (GO:0005125) signatures were significantly down-regulated in TNK2-overexpressing KPC#3 and L3.7 cells (Supplementary Fig. 11d, e; Supplementary Data 9, Supplementary Data 19). Notably, within these signatures, CXCL10, a chemokine known to facilitate CD8<sup>+</sup> T cell recruitment<sup>18,32</sup>, was consistently downregulated in both KPC#3 and L3.7 cells by TNK2 overexpression (Supplementary

Data 9, Supplementary Data 19). The downregulation of CXCL10 by TNK2 in KPC#3 and L3.7 cells was confirmed by qRT-PCR (Supplementary Fig. 11f), and was consistent with a previous study reporting that TNK2 inhibits CD8<sup>+</sup> T cell recruitment by reducing CXCL10 in human prostate cancer cells<sup>18</sup>. Furthermore, deconvolution analysis of the TCGA-PDAC dataset demonstrated that TNK2 levels correlated with reduced CXCL10 expression in PDAC patient samples (Supplementary Fig. 11g). Consistently, correlation analysis of the single-cell RNA sequencing dataset GSE202051 ( $n = 43$ ) also revealed a similar negative correlation between TNK2 and CXCL10 expression specifically in tumor cells (Supplementary Fig. 11h). These results, together with our observation that TNK2 expression is negatively correlated with CD8<sup>+</sup> T cell infiltration (as shown by CD8<sup>+</sup> T cell abundance and their proximity to tumor cells) in human PDAC sample (Fig. 2d–k), suggest that TNK2/ACK1 inhibits CD8<sup>+</sup> T cell infiltration in PDAC by suppressing CXCL10 expression in both mice and humans.

### HVEM interacts with BTLA to mediate TNK2/ACK1-induced CD8<sup>+</sup> T cell inhibition

Next, we investigated the mechanism by which TNK2/ACK1-induced HVEM impairs CD8<sup>+</sup> T cell activity in PDAC. Since B and T lymphocyte attenuator (BTLA) is a well-known receptor on CD8<sup>+</sup> T cells that negatively regulates their activity<sup>33</sup>, we hypothesized that the HVEM-BTLA interaction is responsible for TNK2/ACK1-mediated inhibition of CD8<sup>+</sup> T cells. Analysis of the expression pattern of BTLA in the PDAC microenvironment, using single-cell sequencing data from both human pancreatic cancer samples and KPC mouse spontaneous tumor models (GSE129455), revealed that BTLA was predominantly expressed on T cells, particularly CD8<sup>+</sup> T cells (Supplementary Fig. 12a–d). Additionally, deconvolution analysis of the TCGA dataset indicated that patients with high BTLA expression in CD8<sup>+</sup> T cells had significantly worse prognoses than those with low BTLA expression (Supplementary Fig. 12e), suggesting an important role for CD8<sup>+</sup> T cell-expressed BTLA in PDAC progression.

In direct co-culture of CD8<sup>+</sup> T cells and KPC cells with overexpression or knocked down of TNK2, we observed a significant increase in the proportion of BTLA<sup>+</sup> CD8<sup>+</sup> T cells after co-culture with TNK2-overexpressing KPC#3 cells, while a notable reduction in BTLA<sup>+</sup> CD8<sup>+</sup> T cells was observed in co-culture with TNK2-knockdown KPC#3 cells, as compared to respective controls (Supplementary Fig. 12f, g). Consistently, in an orthotopic allograft tumor model of KPC#3 cells, the proportion of BTLA<sup>+</sup> CD8<sup>+</sup> T cells was significantly higher in tumors overexpressing TNK2, but significantly lower in tumors with TNK2 knockdown, as compared to control tumors (Supplementary Fig. 12h, i). These findings were further corroborated by multiplex immunofluorescence staining of TNK2, CD8, and BTLA in our cohort of 98 human PDAC samples, which demonstrated a significantly higher proportion of BTLA<sup>+</sup>CD8<sup>+</sup> T cells in samples with high TNK2/ACK1 expression compared to those with low TNK2/ACK1 expression (Supplementary Fig. 12j, k). To specifically assess the relationship between TNK2 expression in tumor cells and BTLA expression in CD8<sup>+</sup> T cells in patient samples, we performed a refined deconvolution analysis of the TCGA-PDAC dataset, which revealed a significant positive correlation between tumor-specific TNK2 expression and BTLA expression in CD8<sup>+</sup> T cells (Supplementary Fig. 12l). To further validate this association at single-cell resolution, we analyzed two independent scRNA-seq datasets (CRA001160,  $n = 24$ ; GSE202051,  $n = 43$ ). In both datasets, TNK2 expression in tumor cells was positively correlated with BTLA expression in CD8<sup>+</sup> T cells (Supplementary Fig. 12m, n). Thus, these results indicate a positive association between TNK2/ACK1 expression and BTLA<sup>+</sup>CD8<sup>+</sup> T cell abundance in PDAC. To further elucidate the role of BTLA in TNK2/ACK1-mediated inhibition of CD8<sup>+</sup> T cells, we employed anti-BTLA antibody ( $\alpha$ BTLA) to deplete BTLA in the co-culture of CD8<sup>+</sup> T cells and KPC#3 cells overexpressing TNK2. BTLA blockade effectively abolished TNK2/ACK1-mediated inhibition of

CD8<sup>+</sup> T cells, as evidenced by a significant increase in the proportion of Granzyme B<sup>+</sup> and IFN- $\gamma$ <sup>+</sup> cytotoxic CD8<sup>+</sup> T cells (Supplementary Fig. 13a–c), along with a reduction in PD-1<sup>+</sup> and Tim3<sup>+</sup> exhausted CD8<sup>+</sup> T cells (Supplementary Fig. 13d–f). Furthermore, we evaluated the role of BTLA in antigen-specific CD8<sup>+</sup> T cell-mediated tumor killing by performing BTLA blockade in the co-culture of CD8<sup>+</sup> T cells from OT-1-tt-Tomato mice and KPC#3 cells overexpressing OVA. Notably, BTLA blockade alleviated TNK2/ACK1-mediated suppression of CD8<sup>+</sup> T cell cytotoxicity, as indicated by increased tumor cell apoptosis (Supplementary Fig. 13g–k) and enhanced CD8<sup>+</sup> T cell-mediated tumor cell lysis (Supplementary Fig. 13l). Taken together, these findings underscore the pivotal role of the HVEM-BTLA interaction in mediating TNK2/ACK1-induced inhibition of CD8<sup>+</sup> T cell function in PDAC.

### TNK2/ACK1 facilitates HVEM transcription by directly phosphorylating and activating STAT5a

We next investigated how TNK2/ACK1 promotes the expression of HVEM in PDAC cells. Since TNK2/ACK1 functions as a non-receptor tyrosine kinase that directly phosphorylates target proteins<sup>27,34,35</sup>, we analyzed TNK2-overexpressing and control KPC#3 cells for phosphorylated proteins and TNK2/ACK1-interacting proteins using mass spectrometry analysis, to identify proteins that may be directly phosphorylated by TNK2/ACK1. Through intersection analysis, we identified 4 TNK2/ACK1-interacting proteins, STAT5a, RTN4, FLNB, and WRN, that were phosphorylated in TNK2-overexpressing cells (Fig. 6a, Supplementary Data 10, Supplementary Data 11). Given the enrichment of the phospho-proteins in the Jak-STAT pathway in TNK2-overexpressing cells (Supplementary Fig. 14a), we reasoned that TNK2/ACK1 may directly phosphorylate STAT5a, a STAT family transcription factor<sup>36</sup>, to activate the transcription of HVEM. To confirm the interaction between TNK2/ACK1 and STAT5a, we transiently overexpressed flag-TNK2 and c-myc-STAT5a in HEK-293T cells, followed by immunoprecipitation using anti-flag or c-myc antibodies. Remarkably, exogenous TNK2/ACK1 and STAT5a were co-immunoprecipitated with each other (Fig. 6b). Similarly, endogenous TNK2/ACK1 and STAT5a co-immunoprecipitated with each other in KPC#1 cells and SW1990 cells (Supplementary Fig. 14b). Furthermore, ectopic expression of TNK2 in murine and human PDAC cell lines (KPC#3, L3.7) increased HVEM expression and dramatically facilitated the phosphorylation of STAT5a at the Y694 site, while knockdown of TNK2 (KPC#1, SW1990) reduced the level of HVEM and markedly inhibited the STAT5a-Y694 phosphorylation (Fig. 6c, Supplementary Fig. 14c). Additionally, co-transfection of the full-length TNK2, but not its kinase-dead mutant (TNK2-K158R) or N-terminal deletion mutant (TNK2- $\Delta$ N) in HEK-293T cells, effectively induced the phosphorylation of STAT5a at the Y694 site (Supplementary Fig. 14d). Consistently, IHC staining revealed a significant positive correlation between the expression of TNK2/ACK1 and the phosphorylation of STAT5a in PDAC tissues in our cohort of 98 patients (Supplementary Fig. 14e), suggesting that TNK2/ACK1 may contribute to STAT5a phosphorylation in human tumors. As recombinant proteins for TNK2/ACK1 and STAT5a are not currently available due to their large sizes, we immunoprecipitated STAT5a, TNK2/ACK1, TNK2/ACK1-K158R, and TNK2/ACK1- $\Delta$ N from HEK-293T cells using antibodies against their respective tags, and performed in vitro kinase assays to validate the direct phosphorylation of STAT5a by TNK2/ACK1. We found that full-length TNK2/ACK1 phosphorylated STAT5a, whereas TNK2/ACK1-K158R and TNK2/ACK1- $\Delta$ N had no impact on its phosphorylation (Fig. 6d). Thus, these results indicate that TNK2/ACK1 can directly bind to and phosphorylate STAT5a-Y694 in PDAC cells.

In an effort to investigate the contribution of STAT5a to TNK2/ACK1-induced HVEM expression, we found that STAT5a knockdown reduced HVEM expression in TNK2-overexpressing KPC#3 cells (Fig. 6e). Furthermore, treatment of TNK2-overexpressing KPC#3 cells with staflin, a specific small molecule inhibitor of STAT5a, blocked the

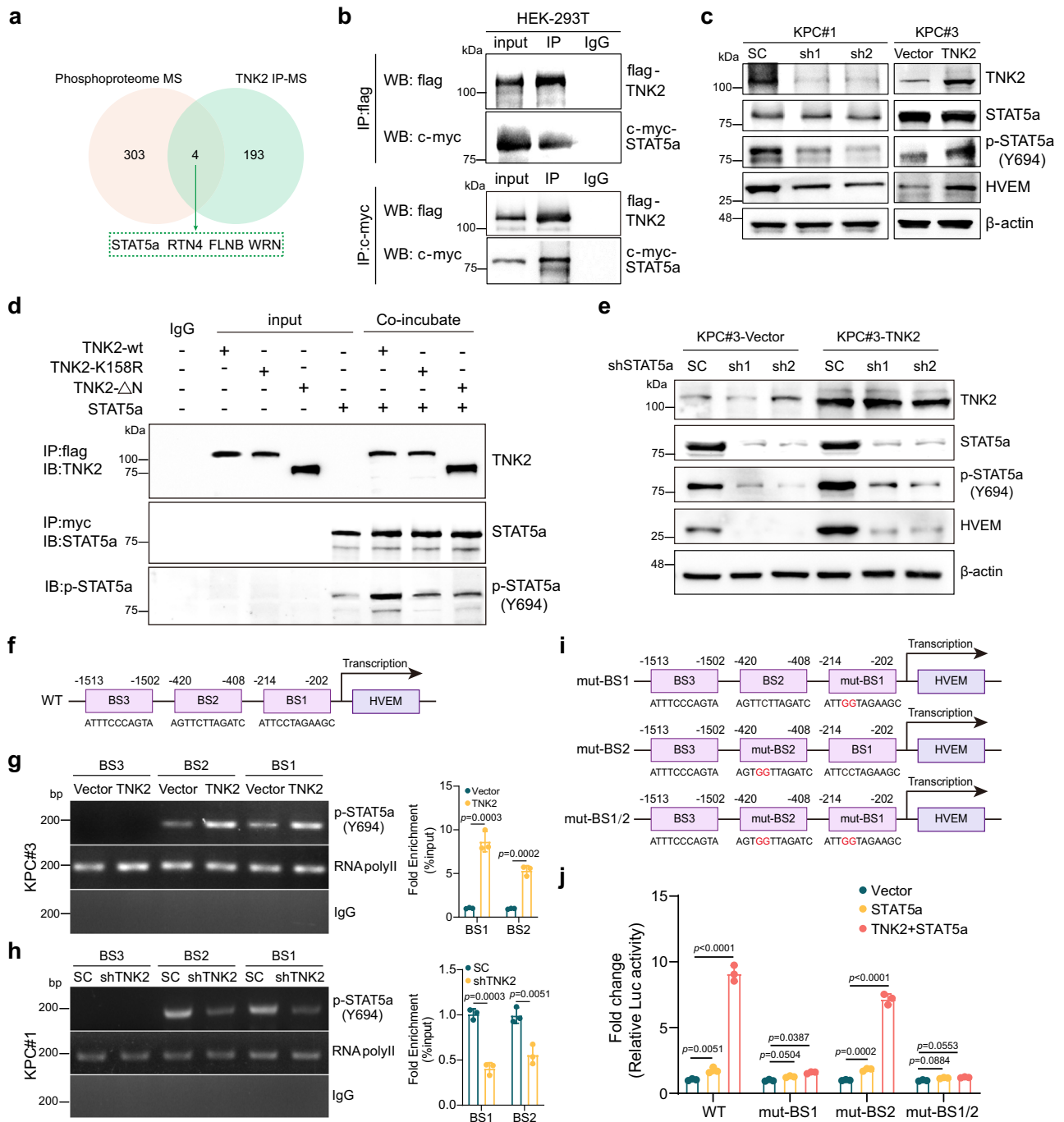


**Fig. 6 | TNK2 activates STAT5a to regulate HVEM gene transcription.** **a** The Venn diagram illustrating the strategy for the screening of the candidate genes encoding proteins phosphorylated by TNK2. **b** The co-immunoprecipitation assay coupled with western blotting showing the interaction between overexpressed TNK2 and STAT5a in HEK-293T cells. **c** Western blotting analysis of indicated protein expression in related KPC cell lines. **d** Western blotting analysis of indicated proteins in *in vitro* kinase assays for measuring the activity of wild type and mutant TNK2 using STAT5a as substrate. **e** Western blotting analysis of indicated proteins in related KPC cell lines. **f** A schematic diagram showing the potential binding sites of STAT5a on the mouse HVEM promoter. **g, h** ChIP-qPCR analysis of the binding of STAT5a to the 3 potential binding sites on the HVEM promoter in indicated KPC cell lines ( $n = 3$  independent experiments). **i** A schematic diagram showing the mutations in the binding sites of STAT5a on the mouse HVEM promoter. **j** The dual luciferase analysis of the reporters containing wild type and the STAT5a binding site mutants of the HVEM promoter co-transfected into HEK-293T cells with TNK2, STAT5a or both ( $n = 3$  independent experiments). Statistical significance was determined by two-tailed unpaired Student's *t* test. Data represent as mean  $\pm$  s.d. Source data are provided as a Source Data file.

induction of HVEM expression by TNK2/ACK1 in a concentration-dependent manner (Supplementary Fig. 14f). These findings indicate that STAT5a is necessary for TNK2/ACK1-induced HVEM expression.

Subsequently, we explored the mechanism by which STAT5a induced HVEM expression. Since STAT5a is a sequence-specific

transcription factor, we identified three STAT5a binding sites in the -2kb region of both murine and human HVEM gene promoters (Fig. 6f, Supplementary Fig. 14g). Chromatin immunoprecipitation (ChIP) experiments demonstrated that p-STAT5a bound to the first and second binding sites on the murine HVEM gene promoter in mouse KPC

cells, which was markedly enhanced by TNK2 overexpression and inhibited by TNK2 knockdown (Fig. 6g, h). Moreover, dual-luciferase assay in HEK-293T cells unveiled that STAT5a significantly enhanced the activity of the HVEM promoter under conditions of TNK2 overexpression, which was completely blocked by the mutation of the first binding site, but not by that of the second binding site (Fig. 6i, j), suggesting that STAT5a binds to the first site (BS1) and second (BS2) site on the promoter of the mouse HVEM gene, but only the binding to BS1 is necessary for activating its transcription. Consistent with these findings, the phosphorylation level of STAT5a in PDAC tissues exhibited a significant positive correlation with the protein level of HVEM in our cohort of 98 cases (Supplementary Fig. 14h). Correlation analysis in the CPTAC proteomic dataset also revealed significant positive associations among TNK2/ACK1, p-STAT5a, and HVEM, and no correlation was observed between TNK2 and total STAT5a protein levels. (Supplementary Fig. 14i–l). Additionally, deconvolution analysis of the TCGA dataset indicated that patients with high STAT5a or HVEM expression in tumor cells had significantly worse prognosis than those with low expression (Supplementary Fig. 14m, n). In summary, the above results demonstrate that TNK2/ACK1 induces HVEM expression by directly binding to and phosphorylating STAT5a, which in turn activates the HVEM gene transcription, leading to inhibition of CD8<sup>+</sup> T cell functions, immune evasion, and progression of PDAC.

### Targeting TNK2/ACK1 reverses PDAC immunosuppression and synergizes with $\alpha$ PD-1 immunotherapy

Our findings have underscored a crucial role of TNK2/ACK1 in inhibiting CD8<sup>+</sup> T cell function, suggesting that targeting TNK2/ACK1 could be a promising strategy to restore CD8<sup>+</sup> T cell-mediated tumor cytotoxicity and reverse the immunosuppressive microenvironment, thereby improving PDAC prognosis. AIM100 and (R)-9b are the two most commonly used small-molecule inhibitors of TNK2/ACK1. AIM100 has been shown to directly suppress TNK2/ACK1 kinase activity and induce its degradation, while (R)-9b was designed as a selective small-molecule inhibitor of TNK2/ACK1 and has the potential to modulate the TME<sup>18,28,37–40</sup>. Treatment with AIM100 or (R)-9b dramatically inhibited TNK2/ACK1 phosphorylation and protein expression levels in KPC#1 cells, accompanied by reduced STAT5a phosphorylation and HVEM expression in a dose-dependent manner (Supplementary Fig. 15a). Similarly, reduced TNK2/ACK1 expression and phosphorylation, decreased STAT5a phosphorylation and diminished HVEM protein levels were observed in both orthotopic xenografts derived from KPC#1 cells and PDAC GEMM models in KPC mice, upon treatment with AIM100 or (R)-9b (Supplementary Fig. 15b, c). Furthermore, flow cytometry analysis revealed that both AIM100 and (R)-9b significantly enhanced the activity and mitigated the exhaustion of CD8<sup>+</sup> T cell co-cultured with KPC#3 cells, but showed no significant impact on the activity of CD8<sup>+</sup> T cells cultured alone (Supplementary Fig. 15d–i). In addition, TNK2/ACK1 inhibition markedly enhanced the cytotoxicity of OT-I-derived CD8<sup>+</sup> T cells against OVA<sup>+</sup> KPC#1 cells, as indicated by enhanced CD8<sup>+</sup> T cell-mediated tumor cell lysis (Supplementary Fig. 15j) and increased tumor cell apoptosis (Supplementary Fig. 15k–n). Therefore, these results confirm that TNK2/ACK1 inhibitors effectively reduce TNK2/ACK1 expression and activity both *in vitro* and *in vivo*, and inhibit the downstream STAT5a signaling, leading to enhanced cytotoxic activity of CD8<sup>+</sup> T cells.

To assess whether TNK2/ACK1 inhibitors reverses the immunosuppressive microenvironment of PDAC and synergizes with ICB therapy, we first established pancreatic orthotopic allograft models using KPC#3 cells in C57BL/6 mice and treated them with AIM100 and  $\alpha$ PD-1, alone or in combination. While AIM100 monotherapy attenuated the growth of allograft tumors and extended the overall survival of tumor-bearing mice, combination with  $\alpha$ PD-1 synergistically suppressed tumor growth and prolonged survival, with a ZIP synergy score of 24.430 (Supplementary Fig. 16a–f). Flow cytometry revealed

AIM100 markedly increased CD8<sup>+</sup> T cell infiltration within the TME, enhanced cytotoxic activity and mitigated exhaustion of CD8<sup>+</sup> T cells, particularly when combined with  $\alpha$ PD-1 therapy (Supplementary Fig. 16g–j). Same results were obtained in the KPC#3 cell-derived subcutaneous allograft models. AIM100 alone inhibited tumor growth and improved mice survival; and these effects were synergistically enhanced when combined with  $\alpha$ PD-1, with a ZIP synergy score of 24.806 (Supplementary Fig. 16k–m). Additionally, AIM100 synergized with  $\alpha$ PD-1 to facilitate CD8<sup>+</sup> T cell infiltration, enhance their cytotoxic activity and impede exhaustion (Supplementary Fig. 16n–q). Overall, these findings demonstrate that the TNK2/ACK1 inhibitor AIM100 effectivity reverses immunosuppressive microenvironment of PDAC, and sensitizes PDAC to  $\alpha$ PD-1 ICB therapy.

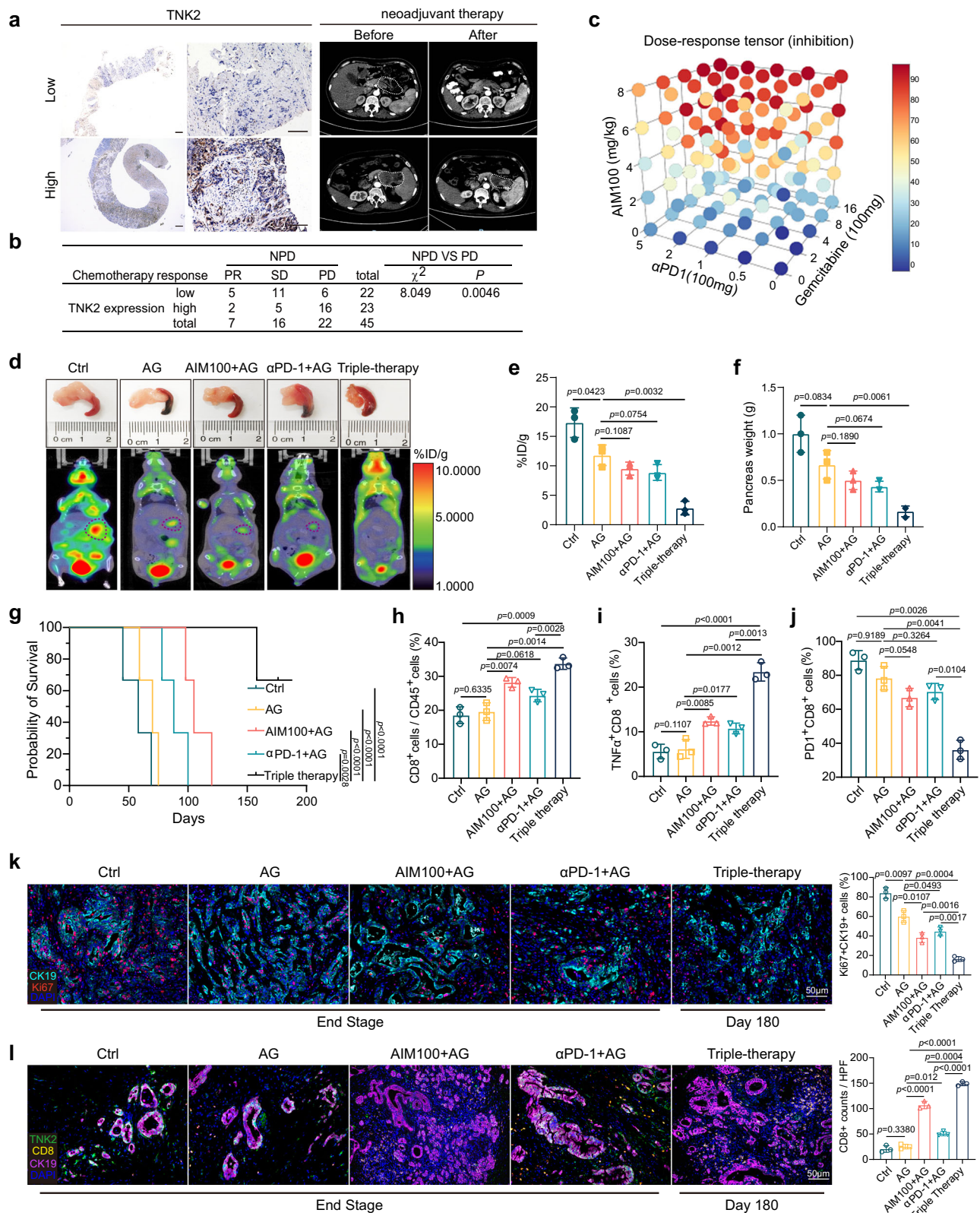
### Combination of TNK2/ACK1 inhibitors, $\alpha$ PD-1, and chemotherapy exhibits promising antitumor effects

Although the current frontline chemotherapy combinations (gemcitabine/nab-paclitaxel or FOLFIRINOX) can inhibit tumor cell growth to a certain extent, the survival prognosis of most patients does not significantly change, possibly related to the immunosuppressive microenvironment of PDAC<sup>41,42</sup>.

Given the close association between TNK2/ACK1 and the immunosuppressive microenvironment, as well as the current limitations of AG treatment strategies, we analyzed pathological tissue samples and pre- and post-treatment imaging data from 45 PDAC patients undergoing the nab-paclitaxel + gemcitabine (AG) regimen as neoadjuvant therapy at TJMUCH, and observed that patients with high TNK2/ACK1 expression at diagnosis had significantly poorer response to AG neoadjuvant therapy than those with low expression (Fig. 7a, b). This suggests that TNK2/ACK1 may also contribute to AG chemotherapy resistance, and that the inhibition of TNK/ACK2 can potentially overcome this resistance through the remodeling of immunosuppressive microenvironment.

To test this hypothesis, we treated KPC#1 cell-derived pancreatic orthotopic allografts in C57BL/6 mice with monotherapy with AG, dual therapy with AIM100 + AG or  $\alpha$ PD-1 + AG, or triple therapy with AIM100 +  $\alpha$ PD-1 + AG (Supplementary Fig. 17a). As compared to the AG monotherapy, both AIM100 + AG and  $\alpha$ PD-1 + AG dual therapies significantly reduced tumor growth, prolonged the overall survival of tumor-bearing mice, and augmented the infiltration and antitumor activity of CD8<sup>+</sup> T cells within the TME, which were further enhanced by the triple combination therapy (Supplementary Fig. 17b–m). Most importantly, analysis of ZIP synergy scoring showed synergistic effects among AIM100, gemcitabine and  $\alpha$ PD-1 on the inhibition of tumor growth (Fig. 7c). Additionally, we treated KPC#1 cell-derived orthotopic allografts in C57BL/6 mice with (R)-9b monotherapy, dual therapies ((R)-9b + AG or (R)-9b +  $\alpha$ PD-1), or triple therapy ((R)-9b +  $\alpha$ PD-1 + AG) (Supplementary Fig. 18a). Compared to the control group, (R)-9b monotherapy significantly reduced tumor growth, prolonged survival, and enhanced CD8<sup>+</sup> T cell infiltration and antitumor activity within the TME. These effects of (R)-9b were further augmented by combination therapies with  $\alpha$ PD-1 or  $\alpha$ PD-1 + AG (Supplementary Fig. 18b–m).

To further validate the therapeutic efficacy of the triple combination therapy for PDAC, we also established spontaneous PDAC models in KPC mice and treated them with AG monotherapy, combined AIM100 and  $\alpha$ PD-1 dual therapy, or triple therapy with AIM100,  $\alpha$ PD-1, and AG when tumors reached a similar volume (50–100 mm<sup>3</sup>) (Supplementary Fig. 19a). Remarkably, ultrasound monitoring, PET-CT scans, and pancreatic weight measurements demonstrated that the triple combination therapy achieved more effective tumor growth inhibition as compared to monotherapy or dual therapies (Fig. 7d–f, Supplementary Fig. 19b, c). Moreover, mice in the triple combination therapy group displayed significantly prolonged survival, with ~66.7% (2 of 3) of the mice still alive at the endpoint (180 days), while all mice



in the other groups had died within 120 days (Fig. 7g). Flow cytometry analysis of tumor tissues revealed that triple combination therapy more effectively promoted CD8<sup>+</sup> T cell infiltration (Fig. 7h), enhanced their antitumor activity (Fig. 7i, Supplementary Fig. 19d, e), and inhibited exhaustion (Fig. 7j, Supplementary Fig. 19f). Consistently, mIHC analysis of tumor tissues indicated that triple combination therapy dramatically inhibited tumor cell proliferation (Fig. 7k,

Supplementary Fig. 19g) and enhanced CD8<sup>+</sup> T cell infiltration (Fig. 7l, Supplementary Fig. 19h).

Additionally, toxicity test in KPC#1 cell-derived orthotopic transplant tumor models showed no significant adverse reactions in the triple combination therapy group, as compared to the groups treated with monotherapy or dual therapy and triple combination therapy, with no abnormalities observed in mouse body weight, organ

**Fig. 7 | TNK2 inhibition together with albumin-paclitaxel and gemcitabine boosts  $\alpha$ PD-1 immunotherapy efficacy.** **a** Representative images of TNK2 IHC staining and CT scans in PDAC patients treated with neoadjuvant therapy. **b** Association between TNK2 expression level and neoadjuvant chemotherapy response. Counts of PR, SD and PD are shown for TNK2-low ( $n = 22$ ) and TNK2-high ( $n = 23$ ) tumors (total  $n = 45$  independent experiments). The overall association across the three response categories was tested by Pearson's  $\chi^2$  test (two-sided);  $p = 0.0046$ . For the binary summary, NPD = PR + SD versus PD (comparison indicated in the panel). PR partial remission, SD stable disease, PD progressive disease, NPD non-progressive disease. **c** The synergy score of GEM, AIM100 and  $\alpha$ PD-1 were analyzed through Synergy finder for the treatment of orthotopic transplantation mouse model. The representative tumor images (**d** up) and the representative PET-CT images (**d** down, **e**) of the KPC GEMM mouse which treated with control, AG, AIM100 and AG, AG and  $\alpha$ PD-1, or AG, AIM100 and  $\alpha$ PD-1, at the experimental

endpoint before the therapy ending stage ( $n = 3$  independent experiments). **f** The pancreas weights of the mouse groups described in (**d**) ( $n = 3$  independent experiments). **g** Kaplan–Meier curves for tumor free survival in the mouse groups in (**d**). Flow cytometry analysis showing the proportions of CD8<sup>+</sup> T cells (**h**), TNF $\alpha$ <sup>+</sup>CD8<sup>+</sup> T cells (**i**), and PD-1<sup>+</sup>CD8<sup>+</sup> T (**j**) cells in the mouse groups in (**d**). **k** The representative mIHC images of tumor issues (CK19 in cyan, Ki67 in red, and nuclei in blue) from the mouse groups in (**d**). **l** The representative mIHC images of tumor issues from the mouse groups in (**d**) at the experimental endpoint, with TNK2 stained in blue, CD8 in red, CK19 in purple, and nuclei in blue. Statistical significance was determined by log-rank (Mantel–Cox) test in survival analysis (**g**) or one-way ANOVA followed by Tukey's multiple comparisons test (**e**, **f**, **h–l**). All tests were two sided (**e–l**). Data represent mean  $\pm$  s.d. Source data are provided as a Source Data file.

coefficients or histological morphology of major organs, coagulation indices (APTT and PT) (Supplementary Figs. 20a–h, 21a–h), or routine blood tests (Supplementary Data 12, 13). In blood biochemical tests, almost all indicators were normal as compared to the control group, apart from a slight increase in alkaline phosphatase (ALP), which might be related to the toxicity of AG regimen (Supplementary Data 14, 15).

In conclusion, TNK2/ACK1 inhibitors,  $\alpha$ PD-1 immunotherapy, and AG chemotherapy demonstrate highly synergistic effects, and their combination therapy can effectively suppress PDAC growth, reverse the immunosuppressive TME, and significantly prolong overall survival, representing a promising treatment strategy for PDAC (Supplementary Fig. 22).

## Discussion

Current immunotherapeutic strategies for pancreatic cancer primarily focus on immune checkpoint blockers, particularly anti-PD-1/PD-L1 antibodies. While some patients exhibit sustained responses to immunotherapy, the overall response rate remains relatively low, largely attributed to the immunosuppressive tumor microenvironment characterized by dense stromal fibrosis and limited immune cell infiltration. However, the molecular mechanisms driving the formation of this immunosuppressive microenvironment in PDAC are still unclear. Hence, identifying pivotal drivers of immunosuppressive microenvironment in PDAC and developing new therapeutic approaches are crucial for overcoming immune evasion and immunotherapy resistance, consequently enhancing patient prognosis. Our study, using a combination of bioinformatics analysis and functional studies, provides compelling evidence demonstrating that in PDAC, TNK2/ACK1 is expressed at higher levels in some tumors than the others and the normal tissues, and promotes HVEM gene transcription by directly phosphorylating STAT5a, thereby impairing CD8<sup>+</sup> T cell function and inducing PDAC immune evasion in a cell-cell contact dependent fashion. Furthermore, the TNK2/ACK1 inhibitors AIM100 and (R)-9b reverse the immunosuppressive PDAC microenvironment, inhibit immune evasion, and synergize with  $\alpha$ PD-1 immunotherapy. Additionally, combining TNK2/ACK1 inhibitor with  $\alpha$ PD-1 and AG chemotherapy suppresses PDAC growth, improves the immunosuppressive TME, and prolongs survival more effectively than the TNK2/ACK1 inhibitors alone or the dual therapies, thus offering a promising therapeutic strategy for PDAC (Supplementary Fig. 22).

In tumors, TNK2/ACK1 dysregulation primarily involves abnormal elevation of expression and aberrant activation of kinase activity<sup>13,14,18,28,43</sup>. In this study, we found that the abnormal overexpression of TNK2 in some tumors of PDAC, is likely mediated by multiple mechanisms, one of which might be gene amplification. We observed varying degrees of TNK2 gene amplification, depending on its definition, across several databases (CPTAC, TCGA, UTSW), and in the PDAC patient cohort at TJMUCH (Supplementary Fig. 2a, e). Increased TNK2 gene copy number correlates with higher TNK2/ACK1 expression levels in tumor tissues, lower immune cell infiltration, and

shorter OS and PFS (Supplementary Figs. 2d, f, g, 4m, n), suggesting a potential role of TNK2 gene copy number increase in the formation of the immunosuppressive PDAC microenvironment. Further studies revealed elevated expression of TNK2/ACK1 in PDAC may also be induced by oncogenic KRAS-G12 mutations (Supplementary Fig. 3), which is the most common genetic alteration in PDAC<sup>44,45</sup>. This finding is consistent with the reported roles of the KRAS pathway in the occurrence and development of PDAC, including immune evasion<sup>46,47</sup>. Based on correlational analyses across multiple large-scale datasets and/or experimental validation in KRAS-mutant and wild type PDAC cell lines using pharmacological KRAS inhibitors, the currently available data suggest the KRAS-G12D, G12V, G12R and G12C can contribute to TNK2 upregulation in PDAC cells. However, the involvement of other types of KRAS mutations cannot be ruled out. In particular, the number of samples carrying some of the KRAS mutations in the datasets was extremely low (Supplementary Fig. 3d–i), thus preventing the assessment of correlation. For example, we were unable to show a correlation between KRAS-G12C and TNK2 due to the insufficient sample size in the datasets, although its effect on TNK2 upregulation was demonstrated in a G12C mutant cell line treated with the pan-KRAS inhibitor (Supplementary Fig. 3l). For other KRAS mutations (e.g., G12S and mutations at positions 13, 23, 60 and 62), the sample size was too small for correlational analysis, and we have not had the opportunity to analyze the cell lines containing these mutations. Thus, further studies are needed to define the roles of these relatively rare KRAS mutations in TNK2 regulation.

Despite the correlation between certain KRAS mutations and high TNK2/ACK1 expression, not all cell lines or patient samples carrying these mutations exhibit high TNK2/ACK1 expression. This likely reflects the heterogeneity among the KRAS mutant patients due to individual variations in genetic background, the complexity of KRAS-associated signaling pathways, and the multifactorial regulation of TNK2 expression in PDAC. Additionally, our data indicate that inhibition of ERK resulted in a significant decrease in TNK2/ACK1 expression in KRAS-G12 mutant cell lines (Supplementary Fig. 3n), underscoring the critical role of ERK in oncogenic KRAS mutant-induced TNK2/ACK1 expression. This is consistent with recent studies demonstrating that KRAS mutations regulate downstream gene transcription through activation of the ERK MAPK cascade in PDAC<sup>22,23</sup>. However, the precise role of ERK in TNK2/ACK1 expression and the specific downstream effectors of ERK that directly regulate TNK2 expression remain to be elucidated in future studies.

Our findings demonstrated that TNK2/ACK1 significantly dampened the cytotoxicity of CD8<sup>+</sup> T cells and fosters their exhaustion through direct cell-cell interactions. Meanwhile, our results also indicated that TNK2/ACK1 could hindered the infiltration of CD8<sup>+</sup> T cells into the TME of PDAC (Figs. 2g–i and 3g). A recent publication noted a negative correlation between TNK2 gene expression and immune cell infiltration as well as immunomodulators in non-small cell lung cancer (NSCLC)<sup>48</sup>. Another recent study reported two distinct TNK2/

ACK1 signaling modules operating in castration-resistant prostate cancer (CRPC) cells and T cells, respectively, which are relevant to antitumor immunity. In T cells, TNK2/ACK1 inhibits TCR activation by phosphorylating CSK at Tyr18, maintaining LCK in its inactive conformation and preventing ligand-independent TCR activation. On the other hand, TNK2/ACK1 expressed in CRPC cells suppresses CXCL10 expression, thereby mitigating the infiltration of active T cell in TME<sup>18</sup>. Consistent with this report, we also found that TNK2/ACK1 expressed in PDAC cells suppressed the expression of CXCL10 (Supplementary Fig. 11). Moreover, we demonstrated that PDAC cell-specific TNK2 directly phosphorylates STAT5a, promoting the expression of HVEM, thereby impairing the antitumor activity of CD8<sup>+</sup> T cells via the HVEM-BTLA axis. Our study has thus identified a novel, cell-cell contact-dependent mechanism underlying the role of tumor-specific TNK2/ACK1 in the formation of immunosuppressive TME, in addition to the previously reported one mediated by chemokines. We also found in our study that TNK2 inhibitors enhance CD8<sup>+</sup> T cell cytotoxicity and reduce their exhaustion primarily by targeting tumor cell-intrinsic TNK2/ACK1, because these inhibitors had no significant effect on the activity of CD8<sup>+</sup> T cells cultured alone (Supplementary Fig. 15). This notion is further supported by single-cell sequencing data indicate that TNK2/ACK1 is expressed predominantly in malignant ductal and endocrine cells, moderately in endothelial cells, and minimally in T cells within the PDAC TME (Supplementary Fig. 1a–c). Along with the previously reported ones, our findings illustrate the complexity of TNK2/ACK1 signaling in cancer, suggesting that the effects and downstream pathways of TNK2/ACK1 are highly dependent on the cell type in which it is expressed. These findings suggest that targeting TNK2/ACK1 represents as a promise therapeutic strategy for PDAC in bolstering CD8<sup>+</sup> T cell-mediated tumor killing through multiple mechanisms, including but not limited to increased CD8<sup>+</sup> T cell infiltration and enhanced cytotoxic activity.

HVEM belongs to the tumor necrosis factor receptor superfamily. It plays a crucial role in modulating both innate and adaptive immune responses<sup>29,30</sup>. For example, it regulates T cell activation, survival, and differentiation, as well as dendritic cell maturation and function<sup>30,49</sup>. HVEM can engage multiple ligands/receptors, including lymphotoxin-alpha (LT $\alpha$ ), LIGHT, B and T lymphocyte attenuator (BTLA), and CD160, leading to context-dependent signaling outcomes<sup>50</sup>. Interestingly, HVEM signaling can either promote or inhibit immune responses depending on the ligands/receptors engaged and the cellular context. For instance, HVEM interaction with BTLA negatively regulates T cell activation, whereas interaction with LIGHT promotes T cell co-stimulation<sup>50</sup>. In this study, we demonstrated that elevation of TNK2 expression in PDAC cells promoted HVEM expression, thereby inhibiting the activity of CD8<sup>+</sup> T cells and fostering their exhaustion. Considering the expression of HVEM on other immune and stromal cells and its bidirectional immune regulatory effects, directly targeting HVEM may not be an ideal strategy. While targeting HVEM could alleviate the inhibitory effect of PDAC cells on CD8<sup>+</sup> T cell activity, it might simultaneously hinder the activation of CD8<sup>+</sup> T cells by HVEM expressed on other immune cells, such as dendritic cells and macrophages, potentially resulting in reduced therapeutic efficacy. Theoretically, targeting immune inhibitory receptors of HVEM could be a more effective strategy<sup>33,51</sup>.

In melanoma, blocking BTLA signaling augments the proliferation and cytokine production of tumor-specific CD8<sup>+</sup> T cells while simultaneously inhibiting other immune checkpoints, such as TIM-3 and PD-1, thereby synergistically enhancing T cell activity<sup>52</sup>. Consistent with this mechanism, our study provides strong evidence that the HVEM-BTLA interaction plays a critical role in TNK2-mediated suppression of CD8<sup>+</sup> T cells in PDAC (Supplementary Figs. 12, 13). However, given the limited infiltration of effector T cells in the PDAC TME and the presence of additional HVEM inhibitory receptors on these T cells, such as CD160, the anti-tumor efficacy of BTLA inhibitor, either as

monotherapy or in combination with anti-PD-1, may be less pronounced than that of TNK2 inhibition in PDAC. Nevertheless, we believe that targeting BTLA may present a promising therapeutic strategy for enhancing immune responses in PDAC. However, further in-depth investigations are necessary to explore potential therapeutic approaches.

Through proteomics analysis of phosphorylated proteins and TNK2/ACK1 interacting partners, we identified STAT5a as a direct downstream effector of TNK2/ACK1. Our data demonstrated that TNK2/ACK1 directly phosphorylated and activated STAT5a, which in turn activates the transcription of HVEM gene, thereby inhibiting the function of CD8<sup>+</sup> T cells and inducing immune evasion in PDAC. These findings suggest for the first time that STAT5a in PDAC cells contributes significantly to the formation of the immunosuppressive TME, aligning with a recent study which reported that targeting the STAT5a/IDO1 axis could reverse the immunosuppressive microenvironment in NSCLC<sup>53</sup>. It should be noted that the STAT5a pathway is also present in T cells, where it plays a pivotal role in their differentiation and activation. Welte et al. demonstrated that STAT5a interacts with the T cell receptor complex and stimulates T cell proliferation<sup>54</sup>. Additionally, STAT5a is required for antigen-induced eosinophil and T-cell recruitment into the tissue<sup>55</sup>, and regulates T helper cell differentiation by several distinct mechanisms<sup>56</sup>. It was recently reported that STAT5 opposes the transcription factor Tox and rewires exhausted CD8<sup>+</sup> T cells toward durable effector-like states during chronic antigen exposure<sup>54,57</sup>. Overall, our results, together with these prior findings, suggest that STAT5a may have bidirectional effects on immunity, either activating or inhibiting immune responses depending on the cell type in which it is expressed. Hence, unselectively targeting STAT5a may not be an effective strategy for activating anti-tumor immune responses either.

In contrast to HVEM and STAT5a, TNK2/ACK1 is expressed at high levels in PDAC cells as compared to normal pancreatic cells and immune cells in the TME (Supplementary Fig. 1a, b), and thus, targeting TNK2/ACK1 would be a preferred strategy to selectively alleviate the inhibitory impact of the TNK2/ACK1-STAT5a-HVEM axis on CD8<sup>+</sup> T cell activity on PDAC cells, without affecting STAT5a- and HVEM-mediated activation of CD8<sup>+</sup> T cells in other pathways or in other cells. Furthermore, inhibiting TNK2/ACK1 can also promote the recruitment of CD8<sup>+</sup> T cells in the PDAC TME, thereby further enhancing the tumor-killing effect mediated by CD8<sup>+</sup> T cells. Therefore, inhibition of TNK2/ACK1 will likely offer a highly promising therapeutic strategy for PDAC.

While TNK2 is not considered as a cancer driver gene in PDAC, our findings have revealed its important function in shaping the immunosuppressive tumor microenvironment in PDAC. Through both correlative analyses and in vitro and in vivo functional studies, we demonstrate that elevated TNK2/ACK1 expression impairs CD8<sup>+</sup> T cell infiltration and cytotoxicity, contributing to immune evasion. Moreover, high TNK2/ACK1 expression was consistently associated with worse prognosis across multiple independent PDAC cohorts, even though TNK2/ACK1 does not meet the criteria of a prognostic biomarker in certain databases such as the Human Protein Atlas. Our results support the clinical relevance of TNK2/ACK1 as a potential therapeutic target in PDAC and suggest that it plays a critical role in immune suppression regardless whether it qualifies as a cancer driver gene according to the conventional definitions.

In summary, our findings underscore the critical role of TNK2/ACK1 in shaping the immunosuppressive microenvironment and promoting immune evasion in PDAC. Building on this discovery, we have developed a novel combination therapy strategy using the TNK2/ACK1 inhibitor,  $\alpha$ PD-1 immunotherapy, and AG chemotherapy, which demonstrated promising therapeutic efficacy in PDAC animal models. Moving forward, clinical trials could be conducted to further evaluate the therapeutic potential of this combination treatment approach for PDAC.

## Methods

The usage of both specimens and patient information and all animal experiments adhered to the guidelines outlined in the National Institutes of Health Guide for the Care and Use of Laboratory Animals were ethically approved by the Ethics Committee of TJMUCIH. All patients provided written consent to the utilization of their specimens and disease information for future investigations, in accordance with the ethical guidelines of the Helsinki Declaration. And skilled investigators conducted the approved protocol with meticulous care for laboratory animals.

### Human samples collection

A retrospective analysis was performed in 70 pairs of cancer and adjacent tissues and 98 patients who underwent radical R0 resection for PDAC and received histological diagnosis at the Tianjin Medical University Cancer Institute and Hospital (TJMUCIH, China) between July 2011 and April 2015. The data collection included clinicopathological information such as age, gender, histological grade, tumor size, TNM stage, and regional lymph node status. The follow-up rate remained at 100% until the last recorded follow-up date on October 23, 2019. It is important to note that none of these patients underwent neoadjuvant chemotherapy or radiotherapy before the collection of tissue samples. Following the surgical procedure, all patients were subjected to systemic gemcitabine/nab-paclitaxel chemotherapy.

Additionally, data were collected from another retrospective cohort comprising 45 patients diagnosed with advanced PDAC and hypertension, based on pancreatic needle biopsy pathology at TJMUCIH from July 2016 to June 2023. The follow-up rate for this cohort remained at 100% until the last recorded follow-up date on December 31, 2023. Clinicopathological data for the 45 PDAC patients included information on albumin paclitaxel and gemcitabine usage history, as well as the chemotherapy response categorized into partial remission (PR), stable disease (SD), and progressed disease (PD).

### Mouse models and Intervention approaches

All mice were maintained in a temperature-controlled room at  $22 \pm 2$  °C with 40–60% relative humidity under a 12 h light/12 h dark cycle. Animals had ad libitum access to water and transgenic mouse-specific chow (spfbiotech, SPF-F04-001). All procedures followed protocols approved by the Animal Care and Use Committees of Tianjin Medical University Cancer Institute and Hospital.

(1) The genetically engineered mouse model, KPC (LSL-K-Ras LSLG12D/+; LSL-Trp53R172H/+; Pdx1-Cre), was generously provided by Dr. Xueli Bai from the First Affiliated Hospital of Zhejiang University, China. The KPC mice were created through the crossbreeding of LSL-KrasG12D, LSL-Trp53R172H, and Pdx1-Cre mice, resulting in animals harboring a conditional p53 mutation and endogenous mutant Kras-G12D expressed in pancreatic tissue. Diagnosis of spontaneously developed PDAC involved identifying a palpable solid tumor in the left peritoneal cavity, confirmed through ultrasound or MRI scans. Euthanasia was performed when mice exhibited a hunched posture, hyperpnea or dyspnea, ascites, lethargy, and the survival date was documented.

(2) Orthotopic transplantation model: PDAC cells (KPC#1 or KPC#3) derived from KPC mouse pancreatic tumor tissues, were orthotopically injected into the pancreas of 6–8-week-old female syngeneic immunocompetent or CD8<sup>+</sup> T cell-deficient C57BL/6 mice or BALB/c nude mice at a concentration of  $1 \times 10^5$  cells in 40  $\mu$ l Matrigel (Corning, 356234). Tumor growth was assessed through IVIS bioluminescence imaging every 4–5 days.

(3) Subcutaneous xenograft tumor model:  $1 \times 10^6$  KPC#1 or KPC#3 cells in 100  $\mu$ l sterile phosphate-buffered saline were transplanted into the mouse groin subcutaneously. Tumor volume was measured and recorded using vernier calipers every 5 days, the formula used for

calculating tumor volume was volume (V) = length (L)  $\times$  width (W)<sup>2</sup>/2. Survival events were scored when mice lost over 10% body weight, tumor burden reached 2.0 cm in diameter or per absolute survival events.

(4) CD8<sup>+</sup> T cell deficient C57BL/6 mice: 6–8-week-old mice were selected for intraperitoneal injections of 200  $\mu$ g  $\alpha$ -CD8a (Bio X cell, #BE0061) or isotype control (Bio X cell, #BE0090) at three-day intervals, totaling three injections. Peripheral blood samples were collected from the mouse tail, and the clearance efficiency of CD8<sup>+</sup> T cells was assessed using flow cytometry.

(5) tdTomato-OT-1 mice: C57BL/6-Tg (Tcra-Tcrb)1100Mjb/J mice (strain #:003831), referred to as OT-1 mice, were procured from Jackson Laboratories. R26-tdTomato(M-NSG) mice (Cat. NO. NM-KI-232838) were acquired from Shanghai Model Organisms Center, Inc. The tdTomato-OT-1 mice were generated from the crossbreeding of OT-1 mice with R26-tdTomato(M-NSG) mice.

(6) Intervention approaches: For targeted therapeutic treatment experiments, mice with tumors reaching 50–100 mm<sup>3</sup> or 5 days after orthotopic transplanted were randomized to receive the following therapies at the reported doses: received albumin paclitaxel (200  $\mu$ g/100  $\mu$ l per mouse) and gemcitabine (500  $\mu$ g/100  $\mu$ l per mouse) administered via intraperitoneal injection every four days. Additionally, an anti-PD-1 antibody (200  $\mu$ g/100  $\mu$ l per mouse, Bio X Cell, #BE0146) was injected on the 4th, 7th, and 10th days, along with AIM100 (6 mg/kg, MCE, HY-15290) every four days or (R)-9b (25 mg/kg, Sigma-Aldrich, SML2073) every five days through intraperitoneal injection. The control group was given the same dose of sterile PBS or isotype control.

### Cell culture

The human PDAC cell lines AsPC-1, MIA PaCa-2, Panc 10.05, Capan-2, CFPAC-1 BxPC-3 and SW1990, and human embryonic kidney cell line HEK-293T, were purchased from the American Type Culture Collection (ATCC, USA). The human PDAC cell line L3.7 was a gift from Dr. Keping Xie (MD Anderson Cancer Center, Houston, TX). The mouse PDAC cell lines KPC#1, KPC#2, KPC#3 were derived from KPC mouse pancreatic tumor tissues. The authenticity of the cells was verified using short tandem repeat (STR) profiling, and mycoplasma contamination was ruled out. Panc 10.05, MIA PaCa-2, HEK-293T and KPC#1, KPC#2, KPC#3 cells were cultured in Dulbecco's modified eagle medium (DMEM, Gibco) with 10% fetal bovine serum (FBS, Gibco) and 1% Penicillin-Streptomycin (10,000 U/mL, Gibco, 15140122). L3.7, AsPC-1, BxPC-3 and SW1990 cells were maintained in Roswell Park Memorial Institute Medium (RPMI)-1640 (Gibco) supplemented with 10% FBS (Gibco) and 1% Penicillin-Streptomycin (10,000 U/mL). CFPAC-1 cells were maintained in R IMDM (Iscove's Modified Dulbecco's Medium) (Gibco) supplemented with 10% FBS (Gibco) and 1% Penicillin-Streptomycin (10,000 U/mL). All cell cultures were maintained at 37 °C in a CO<sub>2</sub>-incubator with 5% humidity.

### Immunohistochemistry (IHC) staining

IHC staining was performed as previously described<sup>58</sup>, to evaluate TNK2 and HVEM expression in pancreatic cancer tissues. Briefly, slides with paraffin-embedded PDAC specimen were placed in microwave for 3 min at 100% power, and for an additional 15 min at 20% power to ensure complete antigen exposure. Subsequently, the slides were incubated overnight at 4 °C with the primary antibody, and with peroxidase-conjugated secondary antibodies for 90-min at room temperature. Chromogenic reactions were executed using a DAB Substrate Kit (ZSGB, ZLI-9019). Staining intensity was assessed based on the following criteria: 0 (negative), 1 (low), 2 (medium), and 3 (high). Staining percentage was categorized as the following: 0 (0% staining), 1 (1–25% stained), 2 (26–50% stained), 3 (51–100% staining). Evaluation, under a light microscope at  $\times 20$  magnification, was conducted in five random fields. The final IP score was calculated by multiplying the

intensity score by the percentage score. The samples were divided into four grades based on the IP scores: 0 (negative, -), 1–2 (low staining, +), 3–5 (moderate staining, ++), 6–9 (high staining, +++). The IHC scores were determined by two independent, blinded pathologists.

### Multiplex immunohistochemical (mIHC)

mIHC was performed using the Opal 7-Color Manual IHC Kit according to the manufacturer instructions (PerkinElmer, NEL811001KT). The antigen exposure process was carried out as that of IHC. Following incubation with the primary antibody, slides were incubated with Opal Polymer anti-Rabbit HRP working solution for 10 min at room temperature. Excessive wash buffer was removed, and 100  $\mu$ l of Opal Fluorophore Working Solution was dispensed onto each slide, followed by incubation at room temperature for 10 min. TNK2 was labeled by Opal 520, HVEM labeled by Opal 570, CD8 labeled by Opal 690, CK19 labeled by Opal 620 or 690, NKp60 labeled by Opal 540, CD33 labeled by Opal 650, and FOXP3 labeled by Opal 540. Once all targets were identified, DAPI Working Solution was administered for 5 min at room temperature within a humidity chamber. Stained slides were scanned across the entire specimen utilizing the Tissue-Gostics system or BZ-X800 fluorescence microscope (KEYENCE). A slide reviewer systematically gridded and selected regions of interest, capturing tissue heterogeneity in an unbiased manner. Images were then captured using a  $\times 20$  lens, with unstained tissues serving to extract tissue autofluorescence. The images were analyzed using Tissue-Gostics analysis software version 2.4. Closest spatial distance analysis of samples was performed using HALO software.

### Human PDAC organoids

Human PDAC organoids (designated as PDAC#1-6) were established from freshly resected PDAC tissues obtained from TJMUCH. These organoids underwent 3D cultivation in Matrigel with reduced Growth Factor (GFR) (Corning, 356230) using complete organoid media. The media comprised Advanced DMEM/F12 (Gibco, 12634010) supplemented with Noggin (0.1 mg/ml, bioGenous, 807-NOG), R-spondin (1  $\mu$ g/ml, bioGenous, 861-RS1), epidermal growth factor (EGF, 50 ng/ml, Peprotech, AF-100-15), Glutamax (Gibco, 35050061), HEPES (Gibco, 15630080), N2 (Gibco, 17502048), B27 (Gibco, 17504044), N-acetyl-L-cysteine (1 mM, Sigma, A7250), Gastrin (10 nM, R&D, 3006), and fibroblast growth factor 10 (FGF10, 100 ng/ml, bioGenous, 816-FGF). Media were changed approximately every 3 days, and cells were passaged about every 7 days based on growth conditions.

### Immunofluorescence staining of organoids

Organoids were removed and collected from Matrigel using Cell Recovery Solution (Corning, 354253), and fixed in 4% paraformaldehyde for 2 h at room temperature. We then made paraffin-embedded paraffin blocks of the organoids. In brief, 0.2–0.4 g of agarose was melted in 10 ml of PBS in a beaker or small reagent bottle. Approximately 200  $\mu$ l of the melted agarose was transferred into a 1.5 ml EP tube. A small 0.5 ml EP tube was then inserted into the agarose within the 1.5 ml EP tube, creating a circular, pointed groove. Subsequently, the organoid precipitate was carefully positioned at the bottom of the groove, ensuring optimal central embedding. PBS was added to the edge of the agarose groove. The agarose block containing the organoid pellet was dehydrated and embedded, and slices with 5  $\mu$ m thickness were prepared. The mIHC staining procedure was as described as “Multiplex immunohistochemical (mIHC)” in this method, with anti-Ki67 antibody (Abcam, ab1667) labeled by Opal 520, anti-CK19 antibody (Abcam, ab52625) labeled by Opal 570 or anti-TNK2 antibody (Abcam, ab185726) labeled by Opal 690. Subsequently, images were analyzed using the BZ-X800 fluorescence microscope (KEYENCE). The fluorescence intensities were measured by ImageJ, and organoid areas were analyzed using the BZ-X 800 analyzer software (KEYENCE).

### Organoid apoptosis assay

In order to detect the effect of TNK2 expression on the activity of CD8<sup>+</sup> T cells, the organoids were infected with lentiviral particles encoding TNK2 or TNK2 shRNA. Organoids and human PBMCs were co-culture as described previously. In detail, after stimulation by PDAC organoid culture media,  $1 \times 10^5$  of human PBMCs were incubated with CD3/CD28 Dynabeads (Thermo, I1452D) at a 1:1 bead-to-cell ratio and 30 U/ml rIL-2 (PeproTech, 200-02) per well in 96-well plates for 24 h before starting co-culture. PDAC organoids and activated PBMCs were then directly co-cultured at 10:1 ratio on Matrigel (Corning, 356230) coated 96 well plate. At the start of co-culture, a Caspase-3/7 Green Ready Probes™ Reagent (Thermo, R37111) and Hoechst33342 (Thermo, H1399) were added to visualize cells undergoing apoptosis. Apoptotic organoids were imaged by BZ-X800 fluorescence microscope (KEYENCE) and quantified using ImageJ.

### Flow cytometry

The tumors were sliced into small fragments and incubated with 1 mg/ml collagenase IV (Thermo, 17104019) and 50 U/ml DNase I (Thermo, 18047019) at 37 °C for 30 min. After mechanical disaggregation, the samples were filtered using 40  $\mu$ m cell strainers. Single-cell suspensions were stained with fluorochrome-conjugated antibodies against proteins such as Zombie, CD45 (Biolegend, 147714), CD19 (Thermo, 69-0193-82), CD11b (BD, 612977), F4/80 (Biolegend, 123141), CD80 (Biolegend, 104726), CD163 (Thermo, 63-1631-82), Gr-1 (Biolegend, 108412), CD3 (Biolegend, 100236), CD4 (Biolegend, 100544), CD8 (Biolegend, 100706), CD25 (BD, 564322), NK1.1 (Biolegend, 108749), BTLA (Biolegend, 134804), PD-1 (Thermo, 63-9981-82), and TIM3 (Biolegend, 134014).

For intracellular cytokine staining of tumor-infiltrating lymphocytes, cells were stimulated *in vitro* with PMA (50 ng/ml, Sigma, P1585) in the presence of GolgiPlug and GolgiStop (BD, 555029) for 4 h. Subsequently, staining of cell surface proteins was performed as described earlier. Cells were fixed and permeabilized using BD Cytofix/Cytoperm (BD, 554722) and stained with antibodies against IFN- $\gamma$  (Biolegend, 505838), GranzymeB (Biolegend, 396408), and TNF- $\alpha$  (Biolegend, 506329). In the case of intranuclear FOXP3 protein staining, single-cell suspensions were stained with antibodies against cell-surface proteins as mentioned earlier, fixed, and permeabilized using the Transcription Factor Buffer Set kit (BD, 562574), followed by staining with the anti-FOXP3 antibody (Thermo, 46-5773-82).

For cell apoptosis analysis, cells were suspended in the annexin V Binding Buffer and stained with annexin V and PI solution (BD, 556547) for 15 min at room temperature. FACS data were acquired using CytoFLEX LX (BECKMAN). The acquired FACS data were then analyzed using FlowJ V10.

### CD8<sup>+</sup> T cell isolation

Naive mouse CD8<sup>+</sup> T cells were isolated from spleen by filtering the cells through a 40  $\mu$ m pore cell strainer in sterile PBS using the Naive CD8<sup>+</sup> T Cell Isolation Kit (Miltenyi, 130-104-075). Red blood cell lysis buffer (Thermo, 00-4333-57) was used to lyse red blood cells. Total CD8<sup>+</sup> T cells were cultured in T cell medium [RPMI1640 with 10% FBS, 1% pen/strep, 1% MEM non-essential amino acids, 25  $\mu$ M  $\beta$ -mercaptoethanol (Gibco, 21985023), 1 mM HEPES (Gibco, 15630080) and 1 mM sodium pyruvate (Gibco, 11360070) at 37 °C in a humidified 5% CO<sub>2</sub> incubator. CD8<sup>+</sup> T cells were activated for 3 d with CD3/CD28 Dynabeads (Thermo, I1452D) at a 1:1 bead-to-cell ratio and 30 U/ml rIL-2 (PeproTech).

Total CD8<sup>+</sup> T from OT-1-td Tomato mice were isolated as mentioned before and cultured for 3 d in T cell medium with 1  $\mu$ g/ml SIIN-FEKL peptide (IBA LifeSciences) and 30 U/ml rIL-2 (PeproTech, 200-02) before co-cultured with tumor cells.

### The co-culture models of PDAC cells and CD8<sup>+</sup> T cells *in vitro*

(1) A total of  $1 \times 10^4$  KPC cells were seeded in a 24-well plate. For the direct co-incubation model,  $2 \times 10^5$  activated CD8<sup>+</sup> T cells were added

directly into the medium. In the indirect co-incubation model,  $2 \times 10^5$  activated CD8<sup>+</sup> T cells were added to a chamber with a pore size of 0.4  $\mu\text{m}$  placed above the co-culture medium. Following 48 h of co-incubation, flow cytometry was employed to assess IFN- $\gamma$ , GranzymeB, and TNF- $\alpha$  levels in CD8<sup>+</sup> T cells, as well as the percentage of PD-1<sup>+</sup> or TIM3<sup>+</sup> CD8<sup>+</sup> T cells.

(2) For the CFSE staining assay, activated CD8<sup>+</sup> T cells were incubated with 10  $\mu\text{M}$  CFSE dye (BioLegend, 423801) at 37 °C for 15 min prior to co-culturing with KPC cells. After 3 days, the cells were harvested, and the proportion of CFSE-positive cells was analyzed by flow cytometry.

(3) In the T cell cytotoxicity assay,  $1 \times 10^4$  KPC-OVA cells were seeded in a 24-well plate. Caspase-3/7 Green Ready Probes™ Reagent (Thermo, R37111) and Hoechst33342 (Thermo, H1399) were added to the medium before co-culture following addition of  $1 \times 10^5$  activated OT-I-Td-Tomato CD8<sup>+</sup> T cells. After 48 h of co-culture, apoptosis of KPC cells was assessed by flow cytometry or imaging using a BZ-X800 fluorescence microscope (KEYENCE) and quantified with ImageJ.

(4) For the cytotoxicity assay assessing CD8<sup>+</sup> T cell activity based on KPC-OVA cells, 5000 KPC cells in a 100  $\mu\text{l}$  volume were seeded in a 96-well U-bottom ultralow attachment plate. Subsequently, activated OT-I-Td-Tomato CD8<sup>+</sup> T cells were added at a target:effector ratio of 1:10 or 1:20. After co-incubation for 6 h, the supernatant was assayed for lactate dehydrogenase (LDH) content using the LDH Cytotoxicity Assay Kit (Beyotime Biotechnology, C0016) following manufacturer's instructions.

(5) The CD8<sup>+</sup> T cell migration experiment *in vitro* was carried out in a transwell system separated by a polycarbonate membrane with a 5  $\mu\text{m}$  pore size. KPC cells were seeded to the bottom chamber in a 24-well plate, and activated CD8<sup>+</sup> T cells were added to the top chamber. After 24 h of culture, cells at the bottom of the chamber were collected and the number of CD8<sup>+</sup> T cells passing through the membrane was quantified by flow cytometry.

### Plasmid construction and generation of lentiviruses

The full-length human TNK2 (NM\_005781.5), human HVEM (NM\_003820.4), mouse TNK2 (NM\_016788.3) and mouse HVEM (NM\_178931.2) were obtained by PCR amplification and subsequently cloned into pLV-EF1-MCS-IRES-3xFlag-Bsd (Biosettia, USA). Human STAT5a (NM\_003152.4) encoded by pLV2-CMV-3xMyc-Puro was purchased from MiaoLing Bio (Wuhan, China). To establish stable knockdown cell lines, shRNAs for TNK2 and HVEM were designed using the Biosettia shRNA designer tool (<https://biosettia.com/support/shrna-designer/>). The shRNA sequences are available in the Supplementary Data 16.

The following plasmids, pCMV-flag-TNK2-K158R encoding the kinase-dead mutant of TNK2, pCMV-flag-TNK2- $\Delta\text{N}$  plasmid encoding TNK2 with deletion of amino acids 1–385 containing the protein kinase domain, pGL3-HVEM-P, pGL3-mut-BS1, pGL3-mut-BS2, and pGL3-mut-BS1/2, were purchased from Sangon Biotech (Shanghai, China).

The lentiviruses were produced by transfecting subconfluent HEK293T cells with lentiviral vectors and packaging plasmids using lipid transfection reagent. Viral supernatants collected 48 h post-transfection were filtered through 0.45  $\mu\text{m}$  filters, and used to transduce the cell lines, followed by antibiotic selection. Cell pools were obtained and expanded one week later.

### Protein mass spectrometry

To investigate the impact of TNK2 on the membrane protein expression of KPC cells, we initially utilized the Cell Fractionation Kit (CST, #9038) following the manufacturer's instructions, to extract membrane proteins from KPC cells. Protein samples were subjected to mass spectrometry analysis for membrane proteins by Lianchuan Biotech

(Hangzhou, China). The identified peptide sequences were provided in the attached Supplementary Data 8.

To identify downstream phosphorylation targets of TNK2, total protein was extracted from KPC cells and subjected to phosphoprotein mass spectrometry analysis, carried out by Lianchuan Biotech (Hangzhou, China). The identified peptide sequences can be found in the Supplementary Data 10.

### RNA extraction and quantitative RT-PCR

Total RNA was isolated from each specimen using TRIzol reagent (Thermo, 15596026). First-strand cDNA was synthesized using M-MLV Reverse Transcriptase (Takara, 2641A). Quantitative PCR for specific genes were performed with a TransStart Green Q-PCR SuperMix Kit (TransGen, AQ101-01). Levels of genes were normalized to that of GAPDH. Sequences for the primers used in this study are listed in Supplementary Data 17.

### Protein extraction and co-immunoprecipitation assays

Total protein extractions were performed using a protein extraction kit (Thermo, 89901). The protein concentrations were determined using a BCA protein assay kit (Thermo, 23227). 1 mg of total protein from each sample was used for co-immunoprecipitation assays following protocols. Protein co-immunoprecipitation (co-IP) was performed from whole-cell lysates prepared in ice-cold IP Lysis Buffer (Thermo, 87788) supplemented with protease and phosphatase inhibitors. After 15–30 min lysis on ice and clarification (12,000  $\times g$ , 10 min, 4 °C), 10% of each sample was saved as input. The remaining lysate (typically 0.5–2.0 mg total protein in 0.5–1.0 ml) was precleared with Protein A/G magnetic beads (Thermo, 88804) for 30 min at 4 °C, then incubated overnight at 4 °C with 1–3  $\mu\text{g}$  of the indicated primary antibody (normal IgG served as negative control). Immune complexes were captured with 20–40  $\mu\text{l}$  Protein A/G beads for 2 h at 4 °C, washed 3 times with IP lysis buffer, and eluted by boiling in 2 $\times$  SDS-Page loading buffer for 10 min. Inputs and IPs were resolved by SDS-PAGE and analyzed by immunoblotting for the bait and prey proteins. A description of the antibodies used was provided in the Supplementary Data 18.

### Immunoblotting assay

The preparation of total cell extracts and immunoblotting with appropriate antibodies (indicated in Supplementary Data 18) were performed. Whole-cell lysates were prepared in RIPA buffer (Thermo, 89900) supplemented with protease and phosphatase inhibitors. Protein concentrations were determined by BCA assay (Thermo, A55864). Equal amounts of protein were resolved by SDS-PAGE, with prestained markers (Thermo, 26617) used to monitor electrophoretic migration and transfer efficiency. Proteins were transferred to PVDF membranes (Millipore, Cat#IPVH00010), blocked, incubated with primary antibodies overnight at 4 °C, and then with HRP-conjugated secondary antibodies for 1 h at room temperature. Signals were developed using an ECL chemiluminescence kit (Millipore, WBKLS0500) and imaged on ChemiDoc XRS+ chemiluminescence gel imaging system (Bio-Rad).

### Chromatin immunoprecipitation (ChIP)

ChIP assays were conducted with an EZ-ChIP kit (Millipore, 17-371) protocol<sup>59</sup>. Cells were crosslinked with 1% formaldehyde at room temperature for 10 min, and then 125 mM glycine was added to inactivate the formaldehyde. Immunoprecipitation of chromatin extracts containing DNA fragments were performed using specific antibodies. The ChIP-enriched DNA was then uncross linked, and quantitative PCR was performed. Supplementary table lists the antibodies used for this study. Regions of HVEM promoter containing STAT5a binding elements predicted by JASPAR present in immunoprecipitants were

amplified and quantified by quantitative PCR. Primer sequences are available in Supplementary Data 17.

### Dual-luciferase assay

To detect whether STAT5a induced the transcriptional activity of HVEM, pLV2-CMV-3×myc-STAT5a was transiently transfected into HEK-293T cells with pGL3-HVEM-P, pGL3-mut-BS1, pGL3-mut-BS2 and pGL3-mut-BS1/2 plasmids respectively. After 24 h, Dual-Luciferase® Reporter (DLR™) Assay System (Promega, E1910) was employed to measure promoter activity. Results, after normalization to Renilla activity, were expressed as a fold induction relative to cells transfected with the control vector.

### TNK2-activated protein kinase assay

HEK-293T cells transfected with TNK2-wt, TNK2-ΔN, TNK2-K158R, or STAT5a plasmids were washed 3 times with pre-chilled PBS before being lysed on ice for 30 min with IP lysis buffer containing protease and phosphatase inhibitor. Upon complete lysis, the cell lysate was collected and centrifuged (12,000 × *g*) at 4 °C for 15 min. The supernatant was subsequently incubated with either anti-flag-tag mAb or anti-c-myc-tag mAb at 4 °C overnight. After incubation, the sample was co-cultured with agarose at 4 °C for 2 h. Then the sample was centrifuged at 1000 × *g* under 4 °C for 2 min and the supernatant was discarded. The agarose beads were then washed with pre-chilled PBS for 3–5 times to remove any non-specific protein bindings. Finally, the proteins specifically bound to the Agarose beads were eluted with co-IP eluent (Thermo, 26149). After sample denaturation and centrifugation, the isolated TNK2-wt, TNK2-ΔN, or TNK2-K158R was incubated with STAT5a, respectively in kinase reaction buffer (CST, #9802) containing 200 μM ATP (CST, #9804) on ice. After 30 min of incubation at 30 °C, SDS sample loading buffer was added to terminate the reactions. The samples were resolved by electrophoresis and subjected to Western blotting analysis.

### Synergy score analysis

To analyze the synergistic effects of the combination therapy between AIM100 and immunotherapies (αPD-1) or chemotherapies (albumin paclitaxel and GEM) in orthotopic transplantation model, synergy scores were calculated by Synergy finder ver2 (<https://synergyfinder.fimm.fi/>) based on the changes of tumor volume at different times in each indicated group<sup>60</sup>. A synergy score of less than –10 indicates antagonistic interaction; a score between –10 and 10 indicates additive interactions; and a score greater than 10 indicates synergistic interactions.

### DNA FISH

TNK2 amplification was detected through DNA fluorescence in situ hybridization (DNA FISH), and performed as protocols from EXONBIO (Guangzhou, China). The probe of TNK2 were supplied by EXONBIO (Guangzhou, China).

### Single-cell transcriptome sequencing and analysis

Seurat R package was used to screen for differentially expressed genes (DEGs) to obtain trajectories and subclusters with biological significance. UMAP (Uniform Manifold Approximation and Projection) is a non-linear dimensionality reduction technique that maps high-dimensional gene expression data from single-cell RNA sequencing to low-dimensional space. The DEGs were analyzed using UMAP dimensionality reduction analysis in the Seurat R package, and the distribution of cells in space was observed. CellChat software was used for cell heterogeneity communication analysis, including communication based on similarity, pairing, and transcription factors<sup>31</sup>. Specifically, CellChat platform visualized the relationship between individual cells in the cell interaction network and determined the interaction patterns

between each cell and other cells. The raw high-throughput data obtained from single-cell RNA sequencing analysis were subjected to preprocessing, quality control, and data mining using bioinformatics toolkits such as Seurat, Cell Ranger, and CellChat. Statistical analysis was performed using standard parameters, and based on the results of differential expression analysis, statistical significance analysis and graph drawing were carried out.

### Spatial transcriptomics sequencing and analysis

Spatial transcriptomics data were processed with Space Ranger (v2.0 or higher) for alignment to GRCh38/hg38, barcode demultiplexing, and gene counting to generate feature–spot matrices linking spatial coordinates with expression. Downstream analysis in R used Seurat (v4.0) and SPATA2 for quality control (spots with UMIs <1000 or mitochondrial reads >20% removed), normalization by SCTransform, and batch correction with Harmony. Spatial domains were identified with BayesSpace using a neighborhood parameter of 15 and clustering resolutions of 0.6–1.2; spatial autocorrelation and differential expression were evaluated with Moran's I ( $P < 0.01$ ). Cell-type proportions per spot were quantified by Cell2location using integrated single-cell RNA-seq references. Giotto (v1.2) was used for ligand-receptor colocalization analysis (threshold  $P < 0.05$ ) and spatial gene-gradient detection with a trend test model. Results were visualized as spatial heatmaps, cell-type proportion maps, and interaction networks using ggplot2 and SPATA2 3D rendering, and spatial enrichment analysis with Spatial DE identified gene modules with significant spatial patterns.

### Statistical analysis

All data are shown as mean ± SD. IBM SPSS and Prism 9 were used for statistical evaluations. Every experiment was conducted at least three times. Student's *t* test was employed to compare mean values between groups. Median survival time was evaluated using Kaplan–Meier curves, with log-rank tests describing survival time discrepancies among different groups. Correlation between different parameters was analyzed using Spearman rank correlation. For analyzing the differential gene expression in tumor and non-tumor tissues, Wilcoxon signed rank tests were applied. To study the tumor growth in mice, repeated measure two-way ANOVA (tumor volume × time) and post-hoc analysis was carried out. The impact of different risk factors on patient prognosis was examined using Cox's proportional hazard regression model.

### Reporting summary

Further information on research design is available in the Nature Portfolio Reporting Summary linked to this article.

### Data availability

All data are available in the main text or the supplementary materials. The raw single cell RNA sequencing data of twenty-four patients were downloaded from CRA001160 dataset (<https://ngdc.cncb.ac.cn/gsa/browse/CRA001160>). The raw sequencing data of thirteen patients from “The Cancer Institute of Tianjin Medical University and the Hospital” and “Peking University School of Medicine” were deposited in The Genome Sequence Archive for Human (GSA-Human) with the accession number: HRA000433. The raw single cell RNA sequencing data of KPC mouse were downloaded from GSE129455 dataset (<https://www.ncbi.nlm.nih.gov/geo/query/acc.cgi?acc=GSE129455>). The mass spectrometry proteomics data had been deposited to the ProteomeXchange Consortium via the PRIDE<sup>61</sup> partner repository with the dataset identifier PXD055503 and the OMIX, China National Center for Bioinformation / Beijing Institute of Genomics, Chinese Academy of Sciences with the dataset identifier OMIX012271<sup>62,63</sup>. The raw sequence data of whole-exome transcriptome sequencing data (GSA:

CRA019058, CRA025613) reported in this paper have been deposited in the Genome Sequence Archive<sup>64</sup> of National Genomics Data Center<sup>65</sup> that are publicly accessible at <https://ngdc.cnbc.ac.cn/gsa/browse/CRA025613> and <https://ngdc.cnbc.ac.cn/gsa/browse/CRA019058>. The raw spatial transcriptomics data of primary pancreatic cancer tissue were downloaded from GSE111672 dataset (<https://www.ncbi.nlm.nih.gov/geo/query/acc.cgi?acc=GSE111672>). Further inquiries can be directed to the corresponding authors. Source data are provided with this paper.

## Code availability

No code was generated/used in the preparation of this paper.

## References

- Siegel, R. L., Miller, K. D., Wagle, N. S. & Jemal, A. Cancer statistics, 2023. *CA Cancer J. Clin.* **73**, 17–48 (2023).
- Xu, Z.-H., Wang, W.-Q., Lou, W.-H. & Liu, L. Insight of pancreatic cancer: recommendations for improving its therapeutic efficacy in the next decade. *J. Pancreatol.* **5**, 58–68 (2022).
- Fan, J. Q. et al. Current advances and outlooks in immunotherapy for pancreatic ductal adenocarcinoma. *Mol. Cancer* **19**, 32 (2020).
- Kolbeinson, H. M., Chandana, S., Wright, G. P. & Chung, M. Pancreatic cancer: a review of current treatment and novel therapies. *J. Invest. Surg.* **36**, 2129884 (2023).
- Topalian, S. L. et al. Survival, durable tumor remission, and long-term safety in patients with advanced melanoma receiving nivolumab. *J. Clin. Oncol.* **41**, 943–954 (2023).
- Le, D. T. et al. Mismatch repair deficiency predicts response of solid tumors to PD-1 blockade. *Science* **357**, 409–413 (2017).
- Brahmer, J. R. et al. Phase I study of single-agent anti-programmed death-1 (MDX-1106) in refractory solid tumors: safety, clinical activity, pharmacodynamics, and immunologic correlates. *J. Clin. Oncol.* **41**, 715–723 (2023).
- Dayyani, F., Macarulla, T., Johnson, A. & Wainberg, Z. A. Second-line treatment options for patients with metastatic pancreatic ductal adenocarcinoma: a systematic literature review. *Cancer Treat. Rev.* **113**, 102502 (2023).
- O'Reilly, E. M. et al. Durvalumab with or without tremelimumab for patients with metastatic pancreatic ductal adenocarcinoma: a phase 2 randomized clinical trial. *JAMA Oncol.* **5**, 1431–1438 (2019).
- Cancer Genome Atlas Research Network. Integrated Genomic Characterization of Pancreatic Ductal Adenocarcinoma. *Cancer Cell* **32**, 185–203.e113 (2017).
- Zhou, Q. et al. Pancreatic ductal adenocarcinoma holds unique features to form an immunosuppressive microenvironment: a narrative review. *J. Pancreatol.* **5**, 174–185 (2022).
- Hodder, S., Fox, M., Binti Ahmad Mokhtar, A. M., Mott, H. R. & Owen, D. ACKnowledging the role of the Activated-Cdc42 associated kinase (ACK) in regulating protein stability in cancer. *Small GTPases* **14**, 14–25 (2023).
- Mahajan, K. & Mahajan, N. P. ACK1/TNK2 tyrosine kinase: molecular signaling and evolving role in cancers. *Oncogene* **34**, 4162–4167 (2015).
- van der Horst, E. H. et al. Metastatic properties and genomic amplification of the tyrosine kinase gene ACK1. *Proc. Natl. Acad. Sci. USA* **102**, 15901–15906 (2005).
- Mahajan, K. et al. Ack1 tyrosine kinase activation correlates with pancreatic cancer progression. *Am. J. Pathol.* **180**, 1386–1393 (2012).
- Zhu, J. et al. Comprehensive Analysis of the Immune Implication of ACK1 Gene in Non-small Cell Lung Cancer. *Front. Oncol.* **10**, 1132 (2020).
- Kong, D. et al. Identification of an ACK1/TNK2-based prognostic signature for colon cancer to predict survival and inflammatory landscapes. *BMC Cancer* **22**, 84 (2022).
- Sridaran, D. et al. Inhibiting ACK1-mediated phosphorylation of C-terminal Src kinase counteracts prostate cancer immune checkpoint blockade resistance. *Nat. Commun.* **13**, 6929 (2022).
- Singh, A. et al. A gene expression signature associated with “K-Ras addiction” reveals regulators of EMT and tumor cell survival. *Cancer Cell* **15**, 489–500 (2009).
- Hallin, J. et al. Anti-tumor efficacy of a potent and selective non-covalent KRAS(G12D) inhibitor. *Nat. Med.* **28**, 2171–2182 (2022).
- Kim, D. et al. Pan-KRAS inhibitor disables oncogenic signalling and tumour growth. *Nature* **619**, 160–166 (2023).
- Klomp, J. E. et al. Determining the ERK-regulated phosphoproteome driving KRAS-mutant cancer. *Science* **384**, eadk0850 (2024).
- Klomp, J. A. et al. Defining the KRAS- and ERK-dependent transcriptome in KRAS-mutant cancers. *Science* **384**, eadk0775 (2024).
- Sturm, G. et al. Comprehensive evaluation of transcriptome-based cell-type quantification methods for immuno-oncology. *Bioinformatics* **35**, i436–i445 (2019).
- Chouhan, S. et al. TNK2/ACK1-mediated phosphorylation of ATP5F1A (ATP synthase F1 subunit alpha) selectively augments survival of prostate cancer while engendering mitochondrial vulnerability. *Autophagy* **19**, 1000–1025 (2023).
- He, W. et al. Co-targeting of ACK1 and KIT triggers additive anti-proliferative and -migration effects in imatinib-resistant gastrointestinal stromal tumors. *Biochim. Biophys. Acta Mol. Basis Dis.* **1869**, 166690 (2023).
- Mahajan, K. et al. ACK1/TNK2 regulates histone H4 Tyr88-phosphorylation and AR gene expression in castration-resistant prostate cancer. *Cancer Cell* **31**, 790–803.e798 (2017).
- Sawant, M. et al. Epigenetic reprogramming of cell cycle genes by ACK1 promotes breast cancer resistance to CDK4/6 inhibitor. *Oncogene* **42**, 2263–2277 (2023).
- Sedy, J. R. & Ramezani-Rad, P. HVEM network signaling in cancer. *Adv. Cancer Res* **142**, 145–186 (2019).
- Steinberg, M. W., Cheung, T. C. & Ware, C. F. The signaling networks of the herpesvirus entry mediator (TNFRSF14) in immune regulation. *Immunol. Rev.* **244**, 169–187 (2011).
- Jin, S. et al. Inference and analysis of cell-cell communication using CellChat. *Nat. Commun.* **12**, 1088 (2021).
- Limagne, E. et al. MEK inhibition overcomes chemoimmunotherapy resistance by inducing CXCL10 in cancer cells. *Cancer Cell* **40**, 136–152.e112 (2022).
- Wojciechowicz, K., Spodzieja, M. & Wardowska, A. The BTLA-HVEM complex - the future of cancer immunotherapy. *Eur. J. Med. Chem.* **268**, 116231 (2024).
- Mahajan, K. et al. Ack1 mediated AKT/PKB tyrosine 176 phosphorylation regulates its activation. *PLoS One* **5**, e9646 (2010).
- Wu, X. et al. The non-receptor tyrosine kinase TNK2/ACK1 is a novel therapeutic target in triple negative breast cancer. *Oncotarget* **8**, 2971–2983 (2017).
- Verhoeven, Y. et al. The potential and controversy of targeting STAT family members in cancer. *Semin. Cancer Biol.* **60**, 41–56 (2020).
- Zhu, J. et al. Improvement of ACK1-targeted therapy efficacy in lung adenocarcinoma using chloroquine or bafilomycin A1. *Mol. Med.* **29**, 6 (2023).
- Jing, L. et al. ACK1 contributes to the pathogenesis of inflammation and autoimmunity by promoting the activation of TLR signaling pathways. *Front. Immunol.* **13**, 864995 (2022).
- Sorkina, T., Ma, S., Larsen, M. B., Watkins, S. C. & Sorkin, A. Small molecule induced oligomerization, clustering and clathrin-independent endocytosis of the dopamine transporter. *Elife* **7**, e32293 (2018).
- Sridaran, D. & Mahajan, N. P. ACK1/TNK2 kinase: molecular mechanisms and emerging cancer therapeutics. *Trends Pharmacol. Sci.* **46**, 62–77 (2025).

41. Padron, L. J. et al. Sotigalimab and/or nivolumab with chemotherapy in first-line metastatic pancreatic cancer: clinical and immunologic analyses from the randomized phase 2 PRINCE trial. *Nat. Med.* **28**, 1167–1177 (2022).
42. Renouf, D. J. et al. The CCTG PA.7 phase II trial of gemcitabine and nab-paclitaxel with or without durvalumab and tremelimumab as initial therapy in metastatic pancreatic ductal adenocarcinoma. *Nat. Commun.* **13**, 5020 (2022).
43. Prieto-Echague, V., Gucwa, A., Craddock, B. P., Brown, D. A. & Miller, W. T. Cancer-associated mutations activate the nonreceptor tyrosine kinase Ack1. *J. Biol. Chem.* **285**, 10605–10615 (2010).
44. Halbrook, C. J., Lyssiotis, C. A., Pasca di Magliano, M. & Maitra, A. Pancreatic cancer: advances and challenges. *Cell* **186**, 1729–1754 (2023).
45. Buscail, L., Bournet, B. & Cordelier, P. Role of oncogenic KRAS in the diagnosis, prognosis and treatment of pancreatic cancer. *Nat. Rev. Gastroenterol. Hepatol.* **17**, 153–168 (2020).
46. Kumarasamy, V. et al. The extracellular niche and tumor microenvironment enhance KRAS inhibitor efficacy in pancreatic cancer. *Cancer Res.* **84**, 1115–1132 (2024).
47. Pant, S. et al. Lymph-node-targeted, mKRAS-specific amphiphile vaccine in pancreatic and colorectal cancer: the phase 1 AMPLIFY-201 trial. *Nat. Med.* **30**, 531–542 (2024).
48. Zhu, J. et al. Identification of downstream signaling cascades of ACK1 and prognostic classifiers in non-small cell lung cancer. *Aging* **13**, 4482–4502 (2021).
49. Ward-Kavanagh, L. K., Lin, W. W., Sedy, J. R. & Ware, C. F. The TNF receptor superfamily in co-stimulating and co-inhibitory responses. *Immunity* **44**, 1005–1019 (2016).
50. Rodriguez-Barbosa, J. I. et al. HVEM, a cosignaling molecular switch, and its interactions with BTLA, CD160 and LIGHT. *Cell Mol. Immunol.* **16**, 679–682 (2019).
51. Sordo-Bahamonde, C. et al. Beyond the anti-PD-1/PD-L1 era: promising role of the BTLA/HVEM axis as a future target for cancer immunotherapy. *Mol. Cancer* **22**, 142 (2023).
52. Fourcade, J. et al. CD8(+) T cells specific for tumor antigens can be rendered dysfunctional by the tumor microenvironment through upregulation of the inhibitory receptors BTLA and PD-1. *Cancer Res.* **72**, 887–896 (2012).
53. Yang, Y. et al. Targeting the STAT5A/IDO1 axis overcomes radio-resistance and reverses the immunosuppressive tumor microenvironment in NSCLC. *Int. J. Oncol.* **62**, 12 (2023).
54. Welte, T. et al. STAT5 interaction with the T cell receptor complex and stimulation of T cell proliferation. *Science* **283**, 222–225 (1999).
55. Kagami, S. et al. Both stat5a and stat5b are required for antigen-induced eosinophil and T-cell recruitment into the tissue. *Blood* **95**, 1370–1377 (2000).
56. Kagami, S. et al. Stat5a regulates T helper cell differentiation by several distinct mechanisms. *Blood* **97**, 2358–2365 (2001).
57. Arcia-Anaya, D. & Elliott, T. STAT5A antagonizes TOX in CD8(+) T cell exhaustion. *Nat. Rev. Immunol.* **23**, 73 (2023).
58. She, C. et al. Combination of RUNX1 inhibitor and gemcitabine mitigates chemo-resistance in pancreatic ductal adenocarcinoma by modulating BiP/PERK/eIF2 $\alpha$ -axis-mediated endoplasmic reticulum stress. *J. Exp. Clin. Cancer Res.* **42**, 238 (2023).
59. Wu, C. et al. Epigenetic dysregulation of ZEB1 is involved in LMO2-promoted T-cell acute lymphoblastic leukaemia leukaemogenesis. *Biochim. Biophys. Acta Mol. Basis Dis.* **1864**, 2511–2525 (2018).
60. Ianevski, A., Giri, A. K. & Aittokallio, T. SynergyFinder 3.0: an interactive analysis and consensus interpretation of multi-drug synergies across multiple samples. *Nucleic Acids Res.* **50**, W739–W743 (2022).
61. Perez-Riverol, Y. et al. The PRIDE database resources in 2022: a hub for mass spectrometry-based proteomics evidences. *Nucleic Acids Res.* **50**, D543–D552 (2022).
62. Zhang 张思思, S. et al. The GSA family in 2025: a broadened sharing platform for multi-omics and multimodal data. *Genom. Proteomics Bioinform.* **23**, qzaf072 (2025).
63. CNCB-NGDC Members and Partners. Database Resources of the National Genomics Data Center, China National Center for Bioinformation in 2025. *Nucleic Acids Res.* **53**, D30–D44 (2025).
64. Chen, T. et al. The genome sequence archive family: toward explosive data growth and diverse data types. *Genom. Proteom. Bioinforma.* **19**, 578–583 (2021).
65. CNCB-NGDC Members and Partners. Database Resources of the National Genomics Data Center, China National Center for Bioinformation in 2024. *Nucleic Acids Res.* **52**, D18–D32 (2024).

## Acknowledgements

The authors thank Professor Xueli Bai (Department of Surgery, the Second Affiliated Hospital, Zhejiang University, China) for the KPC mouse models. This work was supported by the National Natural Science Foundation of China (grants: 82203019 to C.W., 82472838 and 82272799 to A.C., 82303718 and 82473460 to W.L., 82030092 to J.H., 82072657 to S.G., 82272680 and 82072659 to C.H., 82173295 to T.Z., 82273362 to X.W., 82271895 to Y.F.), Joint Funds of the Natural Science Foundation of Tianjin (No. 25JCLMJCO0140 to C.W.), China Postdoctoral Science Foundation (2022M712388 to C.W.), the National Key Research and Development Program of China (2021YFA1201100 to J.H.), Tianjin Health Research Project (TJWJ2023QN012 to W.L.), Tianjin Key Medical Discipline (Specialty) Construction Project (TJYXZDXK-009A). We thank BioRender (<https://www.biorender.com>) for the illustration platform used to create the schematics; figures were created with under CC-BY 4.0 license (Agreement numbers: DS28V1DMOH, UN28V1EGYC).

## Author contributions

C.W., W.L. and X.H. planned and conducted the experiments. C.W., S.L., Y.X. and Z.S. analyzed the data, and wrote the manuscript. X.L., X.H., Y.Y., X.L. and C.Y. provided technical support. Y.X., Y.Z. and R.A. conducted bioinformatic analysis. Y.C., H.W., Y.W. and H.W. conducted experiments, and provided reagents. Y.F., S.G., N.W. and J.Y. provided experimental advice. P.S. and Y.F. provided oversight, and review the manuscript. A.C., C.H. and J.H., conceived the project, provided oversight, and review the manuscript.

## Competing interests

The authors declare no competing interests.

## Additional information

**Supplementary information** The online version contains supplementary material available at <https://doi.org/10.1038/s41467-025-67197-3>.

**Correspondence** and requests for materials should be addressed to Peiqing Sun, Chongbiao Huang, Antao Chang or Jihui Hao.

**Peer review information** *Nature Communications* thanks Magdalena Huber and the other, anonymous, reviewer(s) for their contribution to the peer review of this work. A peer review file is available.

**Reprints and permissions information** is available at <http://www.nature.com/reprints>

**Publisher's note** Springer Nature remains neutral with regard to jurisdictional claims in published maps and institutional affiliations.

**Open Access** This article is licensed under a Creative Commons Attribution-NonCommercial-NoDerivatives 4.0 International License, which permits any non-commercial use, sharing, distribution and reproduction in any medium or format, as long as you give appropriate credit to the original author(s) and the source, provide a link to the Creative Commons licence, and indicate if you modified the licensed material. You do not have permission under this licence to share adapted material derived from this article or parts of it. The images or other third party material in this article are included in the article's Creative Commons licence, unless indicated otherwise in a credit line to the material. If material is not included in the article's Creative Commons licence and your intended use is not permitted by statutory regulation or exceeds the permitted use, you will need to obtain permission directly from the copyright holder. To view a copy of this licence, visit <http://creativecommons.org/licenses/by-nc-nd/4.0/>.

© The Author(s) 2025

---

<sup>1</sup>Pancreas Center, Tianjin Medical University Cancer Institute and Hospital, Tianjin, China. <sup>2</sup>National Clinical Research Center for Cancer, Tianjin, China. <sup>3</sup>State Key Laboratory of Druggability Evaluation and Systematic Translational Medicine, Tianjin, China. <sup>4</sup>Tianjin Key Laboratory of Digestive Cancer, Tianjin, China. <sup>5</sup>Tianjin's Clinical Research Center for Cancer, Tianjin, China. <sup>6</sup>Department of Pain Management, Tianjin Medical University Cancer Institute and Hospital, Tianjin, China. <sup>7</sup>Cancer Center, The Fifth Affiliated Hospital of Sun Yat-Sen University, Zhuhai, China. <sup>8</sup>Department of Oncology, Children's Hospital Affiliated to Chongqing Medical University, Chongqing, China. <sup>9</sup>School of Medicine, Nankai University, Tianjin, China. <sup>10</sup>Laboratory of Cancer Cell Biology, Tianjin Medical University Cancer Institute and Hospital, Tianjin, China. <sup>11</sup>Department of Cancer Biology, Wake Forest University School of Medicine, Winston-Salem, NC, USA. <sup>12</sup>Atrium Health Wake Forest Baptist Comprehensive Cancer Center, Winston-Salem, NC, USA. <sup>13</sup>These authors contributed equally: Chao Wu, Weishuai Liu, Xiangting Hu, Yongjie Xie, Shengnan Li. ✉ e-mail: [psun@wakehealth.edu](mailto:psun@wakehealth.edu); [chhuang@tmu.edu.cn](mailto:chhuang@tmu.edu.cn); [changantao@tjmuch.com](mailto:changantao@tjmuch.com); [haojihui@tjmuch.com](mailto:haojihui@tjmuch.com)